ACS Catalysis

Research Article

Cite This: ACS Catal. 2018, 8, 11407−11422

pubs.acs.org/acscatalysis

Evidence for the Coordination−Insertion Mechanism of Ethene Dimerization at Nickel Cations Exchanged onto Beta Molecular Sieves

Ravi Joshi, Guanghui Zhang, Jeffrey T. Miller, and Rajamani Gounder*

Charles D. Davidson School of Chemical Engineering, Purdue University, 480 Stadium Mall Drive, West Lafayette, Indiana 47907, United States

Supporting Information

ABSTRACT: The mechanistic origin of alkene dimerization on Ni sites supported on aluminosilicates has been ascribed to both coordination−insertion (i.e., Cossee-Arlman) and metallacycle-based cycles; the latter is often invoked in the absence of externally supplied cocatalysts or activators that generate Ni-hydride or Ni-alkyl species to initiate coordination−insertion cycles. Determining the prevalent reaction mechanism at Ni sites is often complicated by the formation and consumption of alkene dimer products via oligomerization and other parallel reactions (e.g., cracking, isomerization) that occur at Brønsted acid sites on supports. Here, ethene dimerization (453 K) was studied on Beta zeolites synthesized to contain predominantly exchanged Ni^{2+} sites according to site balances determined by cation exchange, and to Ni structure determined by CO infrared, UV−visible, and Ni K-edge X-ray absorption spectroscopies. The catalytic behavior of Ni^{2+} sites was isolated by suppressing contributions from residual H^+ sites on support structures, either by selectively poisoning them with Li^+ cations or NH_4^+ species, or by weakening them using a zincosilicate support. Brønsted acid sites form linear dimers (1-butene, *cis*-2-butene, *trans*-2-butene) in thermodynamically equilibrated ratios, in addition to their skeletal isomers (isobutene) and products of subsequent oligomerization-cracking cycles; hence, isobutene formation rates serve as a kinetic marker for the presence of H^+ sites. After residual H^+ sites deactivate during initial reaction times or when they are suppressed prior to reaction, linear butene isomers form in nonequilibrated ratios that are invariant with ethene site-time, reflecting primary butene double-bond isomerization events catalyzed at Ni^{2+}-derived active sites. Ni-zeolites pretreated in oxidative environments (5 kPa O_2, 773 K) show transient activation periods during initial reaction times at dilute ethene pressures (<0.4 kPa) but not at higher ethene pressures (>0.4 kPa) or in the presence of co-fed hydrogen (5 kPa). This behavior is consistent with in situ ethene-assisted formation of $[Ni(II)\text{-}H]^+$ intermediates, which isotopically scramble H_2−D_2 mixtures (453 K) and are quantified from surface H/D exchange reactions (453 K). Taken together, these findings provide unambiguous evidence for the coordination−insertion mechanism as the dominant route for alkene dimerization at Ni^{2+} cations exchanged onto molecular sieves.

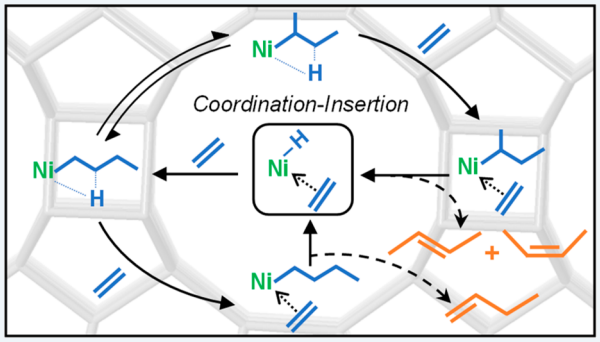

KEYWORDS: *alkene, coordination−insertion, dimerization, ethene, nickel, zeolite*

1. INTRODUCTION

Alkene dimerization is an entry step in oligomerization and chain growth pathways to convert light alkenes into heavier hydrocarbons,[1,2] which provide routes to convert ethene derived from shale gas hydrocarbons (e.g., via ethane steam cracking[3,4]) into chemicals and liquid fuels. Nickel supported on heterogeneous solids including silica,[5,6] silica−alumina,[7,8] zeolites,[9−13] mesoporous materials,[14−17] and sulfated alumina[18−20] are reported to catalyze ethene dimerization in the absence of externally supplied activators or cocatalysts. Such catalysts (e.g., Ni-SiO_2,[6] Ni-SBA-15[21]) have been proposed to operate by the metallacycle mechanism, based on observations that certain homogeneous complexes (e.g., Ni organophosphines[22,23]) also do not require an external initiator and are able to dimerize alkenes by metallacycle-based cycles. In contrast, when cocatalysts (e.g., modified methyl aluminoxane (MMAO)) are used with other classes of Ni-based heterogeneous solids, such as Ni^{2+} cations supported onto metal−organic frameworks (MOFs; e.g., Ni-MFU-4l[24]), ethene dimerization is reported to be catalyzed by the coordination−insertion mechanism (i.e., Cossee-Arlman, degenerate polymerization), as originally proposed for alkene polymerization by Ziegler−Natta catalysts.[25−27] This behavior resembles that of homogeneous α-diimine Ni complexes,[28,29]

Received: August 10, 2018
Revised: October 19, 2018
Published: October 22, 2018

DOI: 10.1021/acscatal.8b03202
ACS Catal. 2018, 8, 11407−11422

which catalyze alkene dimerization once external activators (e.g., alkyl aluminum or boron compounds)[30−32] are added as initiators to form metal−alkyl species.[33] Such activators are also reported to enhance reaction rates but are not required to initiate the coordination−insertion catalytic cycle in the case of certain methallyl Ni catalysts[34] and Shell Higher Olefin Process (SHOP) catalysts,[35] because these form Ni-hydride structures[34] in situ via elimination of ligands bound to the Ni center. Recently, however, isolated Ni^{2+} cations grafted at silanol defects in Beta zeolites were proposed to catalyze coordination−insertion dimerization via Ni-ethenyl-hydride intermediates, without an externally supplied activator.[36]

Mechanistic studies on Ni-based heterogeneous catalysts are complicated, in part because residual Brønsted acid (H^+) sites on supports also catalyze alkene dimerization and isomerization[37−40] to form a mixture of terminal and internal alkene isomers, and in part because Ni^+ sites (Ni-SiO_2,[6] Ni-MCM-41,[41] Ni−X,[5] and Ni−Y[42]), Ni^{2+} sites (Ni-MCM-41,[43] Ni-Beta,[11,13] Ni−X[12]), and $NiOH^+$ sites (Ni-MCM-41[44]) have been purported as candidate precursors to the Ni active sites. Terminal alkene products of ethene oligomerization on Ni-exchanged aluminosilicates (e.g., Y,[45] MCM-22,[9] MCM-36,[9] MCM-41,[43,46] SBA-15,[21] Beta[11,47]) have been proposed to form at Ni^+ cations, while internal alkene isomers have been ascribed to contributions of secondary isomerization at residual H^+ sites. Yet, for ethene oligomerization (393 K, 25 bar C_2H_4) on Ni-exchanged Beta,[13] both terminal and internal alkenes have been proposed to be formed as primary products at Ni^{2+} sites, based on observations that yields of both products increased linearly with conversion.[13]

Here, we study the mechanistic details of ethene dimerization (453 K) at Ni^{2+} cations exchanged onto aluminosilicate Beta zeolites, in the absence of cocatalysts or externally supplied activators, to provide unambiguous evidence supporting the coordination−insertion mechanism. The catalytic contributions of residual Brønsted acid sites on aluminosilicate supports were suppressed by selective prepoisoning with spectator alkali cations (Li^+) or base titrants (NH_4^+) and by weakening their acid strength by using zincosilicate supports. Isobutene, the skeletal isomer of dimer products, serves as a kinetic marker for the presence of H^+ sites during reaction, and its disappearance after deactivation of residual H^+ sites allows identifying butene isomers formed as primary products at Ni-derived active sites. Butenes site-time yields show an activation transient during initial reaction times at dilute ethene pressures (<0.4 kPa), which disappears at higher ethene pressures (>0.4 kPa) or in the presence of co-fed H_2 (5 kPa). These data implicate the formation of $[Ni(II)\text{-}H]^+$ intermediates, whose presence is detected by H/D isotopic scrambling and H_2−D_2 exchange experiments. Taken together, the presence of $[Ni(II)\text{-}H]^+$ intermediates formed in the absence of externally supplied activators, the prevalence of a Ni^{2+} oxidation state by in situ X-ray absorption spectroscopy, and the formation of linear butenes as primary products provide the requisite evidence supporting the coordination−insertion mechanism for ethene dimerization.

2. EXPERIMENTAL SECTION

2.1. Synthesis of Catalysts and Control Samples. Samples are referred to as X-Y-[M]Beta, where X and Y denote the extraframework cations present, and M denotes the framework heteroatom (either Al or Zn). The zincosilicate support Li-[Zn]Beta (CIT-6) was synthesized using a hydrothermal synthesis procedure reported by Takewaki and others.[48] 0.99 g of zinc acetate dihydrate (Sigma-Aldrich, 99.9% pure) and 0.316 g of lithium hydroxide monohydrate (Sigma-Aldrich, 99.95% pure) were added to 46.73 g of ultrapure water (18.2 MΩ cm) and 22.87 g of tetraethylammonium hydroxide (Sigma-Aldrich, 40% (w/w)). The mixture was stirred for ∼0.25 h, until all the solids were completely dissolved. Colloidal silica (22.87 g; Sigma-Aldrich, 40% (w/w)) was then added to the mixture, and it was stirred for 2 h. The final synthesis gel mixture had the following molar composition: 0.65 tetraethylammonium hydroxide (TEAOH)/SiO_2/0.05 $LiOH{\cdot}H_2O$/0.03 $Zn(CH_3COO)_2{\cdot}2H_2O$/30 H_2O. The gel was then transferred to Teflon-lined, stainless steel autoclaves and was heated statically at 413 K for 138 h in a forced convection oven. The product was collected by centrifugation, washed with ultrapure water and acetone, and then dried overnight in an oven at 363 K.

The Ni−Li-[Zn]Beta sample was synthesized by nickel exchange of the Li-[Zn]Beta support using a template ion exchange procedure.[49−51] Nickel exchange was performed at 348 K for 5 h using 100 mL of aqueous 0.1 M $Ni(NO_3)_2$ (Sigma-Aldrich, 99.999%) solution per 1 g of solid catalyst. The pH of the exchange solution was adjusted to 7 at the start using 0.1 N NaOH (Sigma-Aldrich, 99.99%). The exchanged product was collected by centrifugation and washed with ultrapure water. The washed catalyst was dried at ambient temperature in flowing air. The organic template and residual nitrates were removed by treatment in flowing dry air (20 $cm^3\ s^{-1}\ g\text{-}cat^{-1}$, 99.999% ultrahigh purity (UHP), Matheson Tri-Gas) at 853 K (0.0167 K s^{-1}) for 10 h, in a muffle furnace (Nabertherm LE 6/11/P300).

The Ni−H-[Al]Beta sample was synthesized starting from a commercial NH_4-[Al]Beta support (Zeolyst International, CP814E Lot No. 2493-65). The NH_4-[Al]Beta was first converted into H-[Al]Beta by treatment in flowing dry air (1.67 $cm^3\ s^{-1}\ g\text{-}cat^{-1}$, 99.999% UHP, Matheson Tri-Gas) at 773 K (0.0167 K s^{-1}) for 4 h. H-[Al]Beta was subjected to nickel exchange at 348 K for 16 h using 100 mL of aqueous 0.3 M $Ni(NO_3)_2$ (Sigma-Aldrich, 99.999%) solution per gram of solid catalyst. The product was collected by centrifugation and washed with ultrapure water. The washed catalyst was dried at ambient temperature in flowing air. Residual nitrates were removed by treatment in flowing dry air (20 $cm^3\ s^{-1}\ g\text{-}cat^{-1}$, 99.999% UHP, Matheson Tri-Gas) at 773 K (0.0167 K s^{-1}) for 4 h, in the muffle furnace.

The Ni−Li-[Al]Beta was also synthesized starting from commercial NH_4-[Al]Beta support (Zeolyst International, CP814E Lot No. 2493-65). The NH_4-[Al]Beta was first converted into H-[Al]Beta as described above. H-[Al]Beta was subjected to lithium exchange at ambient temperature for 24 h using 100 mL of aqueous $LiNO_3$ (Sigma-Aldrich, reagent grade) solution per gram of catalyst. The pH was periodically adjusted to ∼7 using a 0.1 M LiOH (Sigma-Aldrich, 99.995%) solution. The resulting Li-[Al]Beta was collected by centrifugation, washed with ultrapure water, dried overnight in an oven (363 K), and treated in flowing dry air (20 $cm^3\ s^{-1}\ g\text{-}cat^{-1}$, 99.999% UHP, Matheson Tri-Gas) at 773 K (0.0167 K s^{-1}) for 4 h, in the muffle furnace. The dried Li-[Al]Beta was further subjected to nickel and lithium co-cation exchange at ambient temperature for 24 h using a solution comprising of 0.04 M $Ni(NO_3)_2$ and 0.84 M $LiNO_3$. 100 mL of this solution was used per gram of Li-[Al]Beta, and the pH was periodically adjusted to ∼7 using 0.1 M LiOH solution. The final product

DOI: 10.1021/acscatal.8b03202
ACS Catal. 2018, 8, 11407−11422

Ni−Li-[Al]Beta was collected, washed, dried, and treated in flowing dry air by procedures identical to those for Ni−H-[Al]Beta.

2.2. Characterization. Detailed experimental procedures for X-ray diffraction (XRD), N_2 adsorption, thermogravimetric (TGA) and differential scanning calorimetry (DSC) analysis, scanning electron microscopy (SEM), elemental analysis using atomic absorption spectroscopy (AAS), quantification of H^+ sites using NH_3 temperature-programmed desorption (TPD), and ^{27}Al magic angle spinning nuclear magnetic resonance (MAS NMR) can be found in Section S.2 of the Supporting Information.

IR spectra were collected on a Nicolet 4700 spectrometer with a HgCdTe detector (MCT, cooled to 77 K by liquid N_2) in the range from 4000 to 650 cm^{-1}, by averaging 64 scans at 2 cm^{-1} resolution, and taken relative to an empty cell background reference collected under static vacuum at 303 K. Samples were pressed into self-supporting wafers (0.015−0.02 g cm^{-2}) and then sealed within a custom-built quartz IR cell with CaF_2 windows encased in an alumina silicate ceramic chamber, the design details of which can be found elsewhere.[52,53] Wafer temperatures were measured by K-type thermocouples (Omega) within 2 mm on each side of the wafer. A custom glass vacuum manifold interfacing with the quartz IR cell was used for sample pretreatment and exposure to controlled amounts of gaseous titrants. Prior to each experiment, sample wafers were treated in flowing dry air (6.67 $cm^3\ s^{-1}\ g_{cat}^{-1}$) purified by a Fourier transform infrared (FTIR) purge gas generator (Parker Balston, <1 ppm of CO_2, 200 K H_2O dew point) to 723 K (0.083 K s^{-1}) for 1 h, and then held under dynamic vacuum at 723 K for 1 h. The wafer was then cooled under dynamic vacuum to 423 K for adsorption experiments with pyridine (purified via three freeze−pump−thaw cycles) or to 85 K (using liquid N_2) for adsorption experiments with CO (Matheson, 99.998%). Titrants were admitted to the cell in sequential measured doses, and equilibration of the sample with each dose was considered when the final pressure in the cell and transfer line did not change for 180 s. Titrant dosing was continued until saturation, when detectable features for physisorbed CO (~2133 and 2141 cm^{-1}) and gaseous pyridine (~1600 cm^{-1}) titrant were observed. For doses during subsaturation coverages in which the final pressure was recorded as 0.0 Torr, all of the titrant introduced to the cell was assumed to adsorb on the sample wafer. The acquired IR spectra were baseline-corrected and normalized to combination and overtone modes of zeolite Si−O−Si vibrations (1750−2100 cm^{-1}).

Diffuse reflectance UV−vis spectra were recorded using a Varian Cary 5000 UV−vis−NIR (NIR = near-infrared) spectrophotometer attached with a Harrick Scientific Praying Mantis in situ diffuse reflectance cell. Typically, 0.04−0.05 g of each sample was loaded into the cell and pressed with a microscope slide to obtain a uniform surface. Each spectrum was collected at ambient temperature from 4000 to 52000 cm^{-1} (550 $cm^{-1}\ s^{-1}$) using poly(tetrafluoroethylene) (PTFE; 1 μm powder, Sigma-Aldrich) as the 100% reflectance standard and then converted to an absorption spectrum using the Kubelka−Munk ($F(R)$) function. The spectra were collected on samples (i) first exposed to ambient conditions, (ii) after subsequent dehydration treatment at 673 K (~0.2 K s^{-1}) for 1 h in flowing dry air (20 $cm^3\ s^{-1}\ g_{cat}^{-1}$) followed by cooling to ambient temperature, and (iii) after subsequent hydration treatment at ambient temperature for 0.5 h using a wet air stream (20 $cm^3\ s^{-1}\ g_{cat}^{-1}$, ~3% H_2O) obtained by bubbling dry air through a water saturator at ambient conditions.

X-ray absorption (XAS) measurements at the Ni K-edge (8.3330 keV) were performed on the bending magnet beamline of the Materials Research Collaborative Access Team (MRCAT) at the Advanced Photon Source, Argonne National Laboratory. Photon energies were selected using a water-cooled, double-crystal Si(111) monochromator, which was detuned by ~50% to reduce harmonic reflections. Measurements were made in transmission mode, and data points were acquired in three separate regions: a pre-edge region (−250 to −50 eV, step size = 10 eV, dwell time = 0.25 s), the X-ray absorption near edge structure (XANES) region (−50 to −30 eV, step size = 5 eV, dwell time = 0.25 s and −30 to +30 eV, step size = 0.4 eV, dwell time = 0.5 s), and the extended X-ray absorption fine structure (EXAFS) region (up to 12 $Å^{-1}$, step size = 0.05 $Å^{-1}$, dwell time = 0.5 s). The ionization chambers were optimized for the maximum current with linear response (~1×10^{10} photons s^{-1}) with 10% absorption in the incident ion chamber and 70% absorption in the transmission detector. The X-ray beam was 0.5 × 2.0 mm^2, and data were collected in transmission mode. A third detector in series simultaneously collected a Ni foil reference spectrum with each measurement for energy calibration. Samples were pressed into a cylindrical sample holder consisting of six wells, forming a self-supporting wafer. The sample holder was placed in a quartz reactor tube (1 in. OD, 10 in. length) sealed with Kapton windows by two Ultra-Torr fittings through which gases could be flowed. Samples were analyzed at ambient temperature in He to determine Ni structure under hydrated conditions, and at ambient temperature after treatment at 673 K for 0.5 h in flowing He (111 $cm^3\ s^{-1}\ g_{cat}^{-1}$) to determine Ni structure under dehydrated conditions. To determine oxidation state of Ni under reaction conditions, the dehydrated Ni−Li-[Al]Beta sample was contacted with a stream of 0.07 kPa ethene (278 $cm^3\ s^{-1}\ g_{cat}^{-1}$) obtained by diluting ethene (3% C_2H_4, 97% He, Airgas, 99.999% purity) with He (99.999% UHP, Airgas) at 453 K for 0.25 h and then cooled to ambient temperature to collect the spectrum in the presence of ethene.

The H_2−D_2 isotopic scrambling and exchange experiments were performed using a Micromeritics Autochem II 2920 Chemisorption analyzer connected to a Residual Gas Analyzer (model 200, Stanford Research Systems). Samples were pelleted and sieved to a particle size between 180 and 250 μm. Approximately 0.015−0.020 g of each sample was loaded into a quartz U-tube reactor and supported between two quartz wool plugs. All samples (except for 1% Pt/Al_2O_3) were first treated in flowing dry air (4.2−5.5 $cm^3\ s^{-1}\ g_{cat}^{-1}$, 99.999% UHP, Matheson Tri-Gas) at 803 K (0.167 K s^{-1}) for 5 h and then cooled to 453 K and flushed with Ar for 0.5 h. The 1% Pt/Al_2O_3 sample was first treated in flowing 5% H_2/95% Ar (5.5 $cm^3\ s^{-1}\ g_{cat}^{-1}$, 99.999% UHP, Matheson Tri-Gas) at 673 K (0.167 K s^{-1}) for 1 h and then cooled to 453 K. Following the treatment, signals were continuously recorded for m/z of 2 (H_2), 3 (HD), 4 (D_2), 20 (Ar^{2+}), and 40 (Ar^+). For H/D isotopic scrambling experiments, separate gas mixtures comprising 5% H_2/95% Ar and 5% D_2/95% Ar (99.999% UHP, Matheson Tri-Gas) were combined in different relative amounts in a bypass line to measure feed H_2/D_2/Ar compositions, and then this combined gas stream was flowed over the sample (453 K, 4.2−5.5 $cm^3\ s^{-1}\ g_{cat}^{-1}$), until steady-state signals for H_2, D_2, and HD were obtained. For H/D

DOI: 10.1021/acscatal.8b03202
ACS Catal. 2018, 8, 11407−11422

Table 1. Elemental Composition of Samples in this Study[a]

sample	Ni (wt %)	Si/M	Li/M	Ni/M	H^+/M^b	(cationic charge)/M[c]	Al_f/Al_{tot}[d]
H-[Al]Beta		11.0	0	0	0.65	0.65	0.78
Ni−H-[Al]Beta	1.1	11.0	0	0.20	0.25	0.65	nd
Li-[Al]Beta		11.0	1.01	0	nd	1.01	0.97
Ni−Li-[Al]Beta	1.6	11.0	0.50	0.26	nd	1.02	nd
Li-[Zn]Beta		4.5	0.45	0	nd	0.45	
Ni−Li-[Zn]Beta	1.3	4.5	0.08	0.16	nd	0.40	

[a]M denotes framework metal center (Al^{3+} or Zn^{2+}). nd indicates not determined. [b]Measured by NH_3 TPD. [c]Calculated assuming a 2:1 stoichiometry for Ni^{2+} and a 1:1 stoichiometry for H^+ and Li^+. [d]Measured by ^{27}Al MAS NMR.

surface exchange experiments, the sample was first held in a flowing 5% H_2/95% Ar mixture (4.2−5.5 $cm^3\ s^{-1}\ g_{cat}^{-1}$) at 453 K for 1−2 h, followed by an instantaneous switch to an inlet 5% D_2/95% Ar mixture (4.2−5.5 $cm^3\ s^{-1}\ g_{cat}^{-1}$) using a four-port switching valve (VICI Valco). Then, the sample was held in flowing 5% D_2/95% Ar at 453 K for 1−2 h, after which the flow was switched instantaneously to the 5% H_2/95% Ar mixture. This procedure was repeated 2−3 times (Figures S39 and S41−S44, Supporting Information), and the HD signal was quantified using a response factor relative to an Ar internal standard (m/z = 20), obtained by equilibrating H_2/D_2 mixtures (in Ar) of different composition over a 1% Pt/Al_2O_3 sample at 673 K. The 1% Pt/Al_2O_3 sample was prepared by using a procedure reported elsewhere.[54] The moles of HD formed at Ni sites on Ni−Li-[Al]Beta and Ni−Li-[Zn]Beta were estimated by subtracting the moles of HD formed in equivalent experiments performed on Li-[Al]Beta and Li-[Zn]Beta control samples, respectively (details in Section S.14.6, Supporting Information).

2.3. Measurement of Product Site-Time Yields. The site-time yields of ethene reaction products were measured in a plug-flow tubular quartz reactor at 453 K. Catalyst samples were pelleted and sieved to retain particles between 180 and 250 μm. The amount of sample charged to the reactor was varied between 0.002 and 0.050 g, and samples were diluted with pure-silica Beta (Si-Beta-F) to ensure a minimum of 0.025 g of total solids in the reactor. The catalyst bed was supported in the reactor between two quartz wool plugs. Reactor temperatures were controlled using a resistively heated three-zone furnace (Series 3210, Applied Test Systems) and Watlow controllers (EZ-Zone Series). The temperature of the catalyst bed was measured with a K-type thermocouple in direct contact with the external surface of the quartz tube and positioned at the center of the catalyst bed.

Before measurement of site-time yields, samples (0.01−0.10 g) were treated at 803 K (0.0167 K s^{-1}) in a 5% O_2/95% He mixture (16.7 $cm^3\ g_{cat}^{-1}\ s^{-1}$, 99.999%, Matheson Tri-Gas) for 4 h followed by cooling to 453 K. During this time, the reactant mixture consisting of ethene (1% C_2H_4, 5% Ar, 94% He, Matheson Tri-Gas, 99.999% purity) and He (Pure, Matheson Tri-Gas, 99.999% purity) was transferred to the gas chromatography−mass spectrometry (GC-MS) detector (Agilent 7890B GC; Agilent 5975C MSD) via heated lines (393 K) for calibration purposes. After the catalyst bed was cooled to 453 K, it was treated in pure He flow (16.7 $cm^3\ g_{cat}^{-1}\ s^{-1}$, 99.999%, Matheson Tri-Gas) for at least 0.5 h. The reactant mixture (also containing H_2, in the case of the co-feed experiments) was passed over the catalyst bed under near-ambient pressures, and pressure measurements were recorded using a digital pressure transducer (PX309 series, OMEGA). Reactants and products were separated using GS-AL/KCl capillary column (0.530 mm ID × 50 m; Agilent) and detected using flame ionization detector. The products were identified using the National Institute of Standards and Technology (NIST) spectra library database and also verified by injecting known hydrocarbon standards. Reactants were diluted with He (99.999%, Matheson Tri-Gas) to vary the partial pressure and molar flow rates of ethene (0.01−1 kPa; 1×10^{-7}−10^{-4} (mol ethene) $g^{-1}\ s^{-1}$). In the case of small quantities of catalysts (0.002−0.01 g), they were diluted (1:10 ratio) with pure-silica Beta (Si-Beta-F), which was independently determined to be catalytically inert in the presence of ethene at 453 K. The catalysts were regenerated between consecutive experiments, because they were observed to deactivate with time on stream. The ethene conversion was determined as the ratio of total carbon molar flow rates in products to the total carbon molar flow rates in the ethene feed. The molar selectivities were calculated as the ratio of the site-time yield of given product to that of the total site-time yields of all detected products. The control samples, namely, Li-[Zn]Beta and Li-[Al]Beta, showed undetectable reactivity in the presence of ethene (0.1−1 kPa) at 453 K.

3. RESULTS AND DISCUSSION

3.1. Preparation of Nickel Ion-Exchanged Molecular Sieves. All samples are referred to as X-Y-[M]Beta, where X and Y denote the extraframework cations present, and M denotes the framework heteroatom (either Al or Zn). The H-[Al]Beta sample was prepared by treating an NH_4-[Al]Beta sample in flowing air at elevated temperature (773 K) and was subsequently ion-exchanged with either an aqueous $Ni(NO_3)_2$ solution or an aqueous $LiNO_3$ solution (pH ≈ 7) to obtain the Ni−H-[Al]Beta or Li-[Al]Beta samples, respectively. The Ni−Li-[Al]Beta sample was prepared by simultaneous ion exchange of Li-[Al]Beta with an aqueous solution containing $Ni(NO_3)_2$ and $LiNO_3$ (pH ≈ 7). In the case of the zincosilicate materials, a previously reported hydrothermal procedure[48] was used to synthesize Li-[Zn]Beta, which was then template ion-exchanged[49−51] with an aqueous $Ni(NO_3)_2$ solution to obtain the Ni−Li-[Zn]Beta sample. For all samples, XRD patterns (Figure S1, Supporting Information), micropore volumes (Table S1, Supporting Information) determined from N_2 adsorption isotherms (77 K) (Figures S2 and S3, Supporting Information), ^{27}Al MAS NMR spectra (Figure S5, Supporting Information), and SEM images (Figure S6, Supporting Information) are reported in the Supporting Information.

Table 1 summarizes the elemental composition on each sample determined by AAS, the number of residual H^+ sites quantified by NH_3 temperature programmed desorption (TPD), and the fraction of framework Al atoms (Al_f/Al_{tot}) determined by ^{27}Al MAS NMR. The cationic charge balance

DOI: 10.1021/acscatal.8b03202
ACS Catal. 2018, 8, 11407−11422

((cationic charge)/M, Table 1) on H-[Al]Beta was quantified by TPD after aqueous-phase NH_3 titration of H^+ sites, and on Li-[Al]Beta and Li-[Zn]Beta it was quantified by AAS to measure the total Li content. The cationic charge balances on each parent sample were similar to those on their respective Ni-exchanged forms, which are reported in Table 1 and calculated from the number of residual monovalent (H^+ or Li^+) cations and the number of Ni species on the solid (assuming a 2:1 exchange stoichiometry per divalent Ni^{2+} cation). Furthermore, an elemental balance performed for lithium and nickel present on the parent Li-[Zn]Beta and the Ni−Li-[Zn]Beta solids, and the lithium and nickel present in aqueous solutions before and after the template Ni ion-exchange procedure (Table S3, Supporting Information), were consistent with a 2:1 exchange stoichiometry. The Ni/Al value on Ni−H-[Al]Beta (0.20, Table 1) was identical to the number of divalent Ni^{2+} and Co^{2+} cations exchanged at saturation on the parent H-[Al]Beta sample, which was determined by measuring ion-exchange isotherms (0.20; Figures S7 and S8 Supporting Information). The Ni/Al value on the Ni−Li-[Al]Beta sample (0.26, Table 1) was higher than the total number of divalent cations exchanged onto H-[Al]Beta at saturation (0.20), because of the specific exchange conditions used to prepare this sample.

The higher Ni^{2+} uptake on the Ni−Li-[Al]Beta than the Ni−H-[Al]Beta sample appears to reflect, in part, the higher fraction of tetrahedrally coordinated framework Al sites (Al_f/Al_{tot}, Table 1) present on the parent Li-[Al]Beta (0.97) than the parent H-[Al]Beta (0.78) sample. The H^+/Al_{tot} value was lower (0.65, Table 1) than the measured fraction of framework Al (0.78, Table 1) on H-[Al]Beta, perhaps because partial hydrolysis of Si−O−Al bonds[55] formed some undercoordinated Lewis acidic Al during conditions of aqueous NH_3 titration, which are otherwise detected as tetrahedral species because of the hydration treatments performed prior to collecting ^{27}Al MAS NMR spectra. Such phenomena would be consistent with prior studies on Beta[55,56] and ZSM-5[57] zeolites, in which the replacement of NH_4^+ or alkali cations with H^+ caused the reversible transformation of tetrahedral Al into octahedral Al. Cobalt cations can be exchanged nearly exclusively as divalent Co^{2+}, and saturation Co^{2+}-exchange capacities provide quantitative measurements of zeolite framework Al centers located in close proximity. Co^{2+} cations were introduced onto H-[Al]Beta and NH_4-[Al]Beta by aqueous ion-exchange, and the Co^{2+}-exchange isotherms (Figures S8 and S10, Supporting Information) gave saturation Co/Al values of 0.20 and 0.35, respectively, indicating a lower fraction of Al sites in close proximity[58] on H-form samples in aqueous solution. This finding is consistent with a ^{27}Al multiple quantum (MQ) MAS NMR study of zeolite Beta[59] concluding that framework Al sites in close proximity are more susceptible than isolated Al to undergo partial or complete removal from the zeolite lattice. In the case of Li-[Zn]Beta, the Li/Zn ratio of 0.45 (Table 1) cannot be interpreted at face value, given that both Li^+ and tetraethylammonium (TEA^+) cations charge-balance framework Zn^{2+} during crystallization, that TEA^+ cations decompose to leave behind H^+ sites after subsequent high-temperature treatments (detected from IR spectra of adsorbed CO, Figure S14, Supporting Information), and that framework Zn sites in different configuration require different numbers of Li^+ (0, 1, or 2) for charge-compensation.[60] Taken together, these data are consistent with the predominant exchange of Ni^{2+} cations on Ni−H-[Al]Beta, Ni−Li-[Al]Beta, and Ni−Li-[Zn]Beta, and we next characterize Ni structure and coordination using direct spectroscopic probes.

3.2. Spectroscopic Characterization of Ni Structure and Geometry. Infrared spectra of CO adsorbed (85 K) on Ni−H-[Al]Beta, Ni−Li-[Al]Beta, and Ni−Li-[Zn]Beta are, respectively, shown in Figure 1a−c. All samples were first

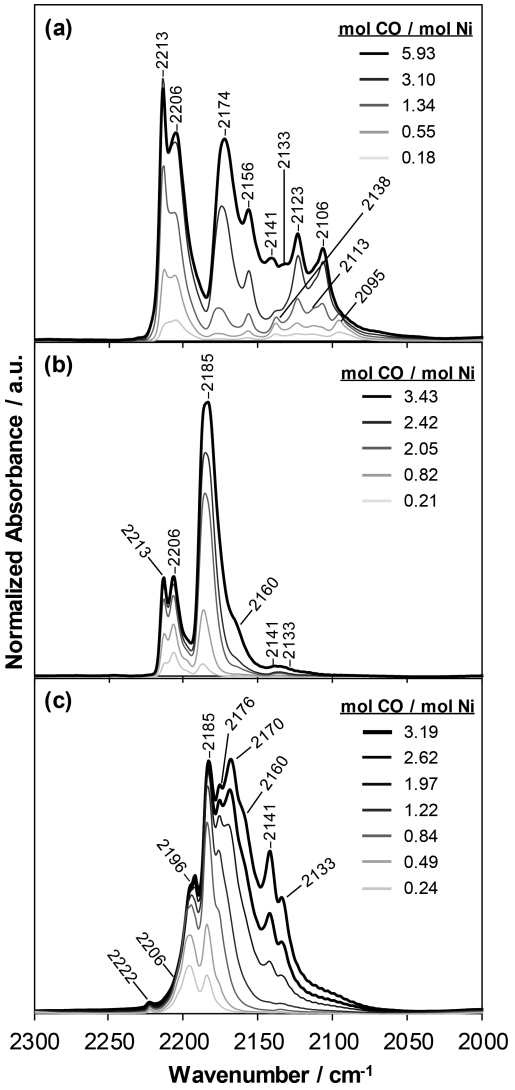

Figure 1. Infrared difference spectra (relative to a vacant surface) with increasing amounts (light to dark) of CO adsorbed at 85 K for (a) Ni−H-[Al]Beta, (b) Ni−Li-[Al]Beta, and (c) Ni−Li-[Zn]Beta. The dark black line indicates spectra collected at saturation coverages (CO/Ni > 1.0; peaks observed at 2133 and 2141 cm^{-1} are for physisorbed CO).

treated in vacuum to 823 K (1 h) and then cooled to 85 K prior to CO exposure. IR spectra were collected with increasing CO coverage, until peaks for physisorbed CO (2133, 2141 cm^{-1})[61,62] and CO adsorbed at silanol groups (2160 cm^{-1})[61,63] were observed. Absorption features for CO on NiO particles supported on Si-Beta-F (ca. 2155 cm^{-1}, Figure S13, Supporting Information)[11,64] or metallic Ni nanoparticles (ca. 2030 cm^{-1})[65,66] were not observed on any sample.

IR spectra of CO adsorbed on Ni−H-[Al]Beta and Ni−Li-[Al]Beta (Figure 1a,b) samples showed peaks centered at 2213

DOI: 10.1021/acscatal.8b03202
ACS Catal. 2018, 8, 11407−11422

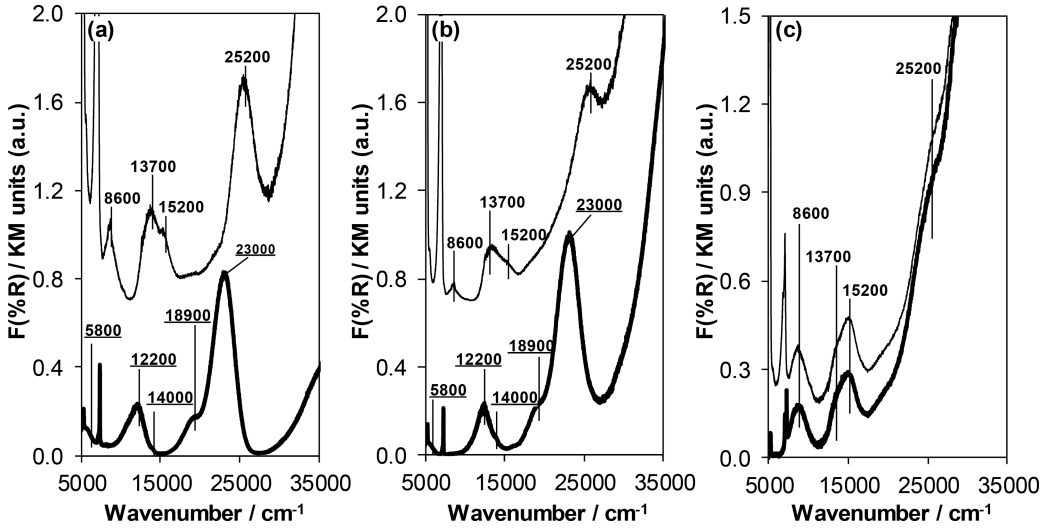

Figure 2. Diffuse reflectance UV−vis spectra collected under hydrated (light traces) and dehydrated conditions (dark traces) for (a) Ni−H-[Al]Beta, (b) Ni−Li-[Al]Beta, and (c) Ni−Li-[Zn]Beta. Underlined and nonunderlined wavenumbers indicate the absorption features for distorted tetrahedral Ni^{2+} cations and for octahedral Ni^{2+} cations, respectively.

and 2206 cm^{-1} for $Ni^{2+}(CO)$ and $Ni^{2+}(CO)_2$ complexes, respectively.[66,67] These peaks were not observed for IR spectra of CO adsorbed on Ni−Li-[Zn]Beta (Figure 1c); however, a predominant feature at 2196 cm^{-1} was observed on this sample. The 2196 cm^{-1} peak appears to correspond to CO adsorbed onto Ni^{2+} cations grafted at silanol defects, as IR peaks of similar frequency have been reported for CO bound to Ni^{2+} cations in nickel-impregnated silica[68] and dealuminated Beta.[67] In the case of zincosilicate Beta, framework Zn centers have been reported to be unstable in air treatment at high temperatures (>823 K).[48] Thus, the air-treatment procedure used here likely removed some framework Zn atoms to form framework vacancy defects, leading to the predominant formation of grafted Ni^{2+} cations. Moreover, the Ni−Li-[Zn]Beta sample showed a small peak centered at 2222 cm^{-1} for a second type of $Ni^{2+}(CO)$ complex that is reported[69,70] to be distinct from the $Ni^{2+}(CO)$ complex at 2213 cm^{-1}. The formation of two types of $Ni^{2+}(CO)$ complexes has been speculated to reflect Ni^{2+} cations located in different locations of Beta[67] and ZSM-5.[69,70]

In addition to features corresponding to Ni^{2+} sites, IR peaks for CO adsorbed at Brønsted acid sites (2174 cm^{-1};[67,71] H-[Al]Beta spectra in Figure S11, Supporting Information) were only observed on Ni−H-[Al]Beta (Figure 1a), while those for CO adsorbed at Li^+ cations (2185 cm^{-1}; Li-[Al]Beta spectra in Figure S12 and Li-[Zn]Beta spectra in Figure S14, Supporting Information) were observed on Ni−Li-[Al]Beta (Figure 1b) and Ni−Li-[Zn]Beta (Figure 1c). In the case of Ni−Li-[Zn]Beta (Figure 1c), the IR peak at 2170 cm^{-1} was also observed on Li-[Zn]Beta (Figure S14, Supporting Information) but not on H-[Al]Beta (Figure S11, Supporting Information) nor on Li-[Al]Beta (Figure S12, Supporting Information), and is assigned to Zn−OH groups. The 2176 cm^{-1} peak observed on Ni−Li-[Zn]Beta (Figure 1c) was also observed on Li-[Zn]Beta (Figure S14, Supporting Information), and is analogous to 2174 cm^{-1} peak for Brønsted sites on H-[Al]Beta (Figure S11, Supporting Information) and Ni−H-[Al]Beta (Figure 1b) and is therefore assigned to minority Brønsted sites in zincosilicates that are proposed to be too weak to protonate pyridine[60] (details in Section S.4.6, Supporting Information).

IR spectra collected at low CO coverages (CO/Ni < 1.0) of Ni−H-[Al]Beta (Figure 1a) also showed peaks centered at 2113 cm^{-1} for $Ni^+(CO)$ and at 2138 and 2095 cm^{-1} for the symmetric and asymmetric modes of $Ni^+(CO)_2$, respectively.[66,67] These IR peaks disappeared with increasing CO coverage (CO/Ni > 1.0), which led to the emergence of new peaks centered at 2106, 2123, and 2156 cm^{-1} corresponding to $Ni^+(CO)_3$ complexes,[66,67] consistent with the conversion of $Ni^+(CO)$ and $Ni^+(CO)_2$ complexes into $Ni^+(CO)_3$. The Ni^+ cations appeared to have formed upon vacuum treatment (823 K, 1 h) by Ni^{2+} auto-reduction phenomena that have reported previously for Ni-exchanged NaY[43] and Ni-impregnated ZSM-5.[70] Higher IR peak intensities for CO at Ni^+ cations in NaY were observed, as the temperature of thermal treatments (air, 8 h) increased from 473 to 823 K,[43] and in ZSM-5 they were observed for samples treated in vacuum (but not in O_2) via mechanisms proposed to occur by consumption of hydroxyl groups.[70] Absorption features for Ni^+ carbonyl complexes were not observed on Ni−Li-[Al]Beta (Figure 1b) or Ni−Li-[Zn]Beta (Figure 1c) samples that contained residual Li^+ cations, suggesting that auto-reduction events may involve H^+ sites. The small intensity of the $Ni^+(CO)$ peak (2113 cm^{-1}) relative to the $Ni^{2+}(CO)$ peak (2213 cm^{-1}) on Ni−H-[Al]Beta (Figure 1c), however, indicates that only a minority fraction of Ni^+ is formed during the vacuum treatment, given that extinction coefficients measured for the $Ni^+(CO)$ peak at 2113 cm^{-1} are reported to be 10 times larger than that for the $Ni^{2+}(CO)$ peak at 2213 cm^{-1}.[72]

Diffuse reflectance UV−visible (DRUV) spectra collected at ambient temperature of Ni−H-[Al]Beta, Ni−Li-[Al]Beta, and Ni−Li-[Zn]Beta are shown, respectively, in Figure 2a−c, when collected under hydrated (light traces) and dehydrated (dark traces) conditions. All samples were first treated in flowing dry air to 673 K (1 h), before cooling to ambient temperature to collect spectra under dehydrated conditions. The samples were then rehydrated in flowing wet air (0.5 h) to collect spectra under hydrated conditions at ambient temperature. The sharp features centered at 5250 and 7200 cm^{-1} for all samples under hydrated conditions (light traces) represent the combination of stretching and bending modes of H_2O and the first overtone of the silanol O−H stretching vibration, respectively.[73,74]

DOI: 10.1021/acscatal.8b03202
ACS Catal. 2018, 8, 11407−11422

The light traces in Figure 2a–c, respectively, show the DRUV spectra of Ni–Li-[Al]Beta, Ni–H-[Al]Beta, and Ni–Li-[Zn]Beta samples collected under hydrated conditions. All three samples showed absorption bands at 8600, 13 700, and 25 500 cm^{-1}, respectively, corresponding to the spin-allowed d–d transitions ($^3A_{2g}(F) \rightarrow {}^3T_{2g}(F)$, $^3A_{2g}(F) \rightarrow {}^3T_{1g}(F)$, $^3A_{2g}(F) \rightarrow {}^3T_{1g}(P)$) of an octahedral $Ni^{2+}(H_2O)_6$ species.[75−78] These samples also showed an additional band at 15 200 cm^{-1} for the spin-forbidden d–d transition ($^3A_{2g}(F) \rightarrow {}^1E_g(D)$) of the $Ni^{2+}(H_2O)_6$ species. This spin-forbidden d–d transition was observed previously for Ni-exchanged Beta[79,80] and FAU[81,82] and was attributed to spin–orbit coupling, which causes the $^1E_g(D)$ and $^3T_{1g}(F)$ levels to become similar in energy.[82] Thus, under hydrated conditions, Ni^{2+} cations on Ni–H-[Al]Beta, Ni–Li-[Al]Beta, and Ni–Li-[Zn]Beta are present in octahedral coordination with oxygen atoms.

The dark traces in Figure 2a–c, respectively, show the DRUV spectra of Ni–Li-[Al]Beta, Ni–H-[Al]Beta, and Ni–Li-[Zn]Beta samples under dehydrated conditions. The Ni–H-[Al]Beta and Ni–Li-[Al]Beta samples showed absorption bands at 5800, 12 200, 14 000, 18 900, and 23 000 cm^{-1}, respectively, corresponding to the spin-allowed d–d transition ($^3T_1(F) \rightarrow {}^3T_2(F)$, $^3T_1(F) \rightarrow {}^3A_2(F)$, and $^3T_1(F) \rightarrow {}^3T_1(P)$ that is split into three components because of tetrahedral distortion[82]) of Ni^{2+} cations in distorted tetrahedral coordination.[82−84] The transformation of Ni^{2+} cations from an octahedral (hydrated) to distorted tetrahedral (dehydrated) geometry is consistent with the predominance of exchanged Ni^{2+} cations in ion-exchange positions of Ni–H-[Al]Beta (Figure 2a) and Ni–Li-[Al]Beta (Figure 2b), consistent with their cation site balances (Table 1) and CO IR spectra (Figure 1). The DRUV spectrum of Ni–Li-[Zn]Beta under dehydrated conditions (Figure 2c, dark trace), however, was similar to that collected under hydrated conditions (Figure 2c, light trace), indicating that Ni^{2+} cations remain predominantly octahedrally coordinated to oxygen atoms. Similar observations of octahedrally coordinated Ni^{2+} cations under ambient and dehydrated conditions have been reported for Ni-exchanged siliceous MCM-41,[51] proposed to contain Ni^{2+} cations grafted at six-membered siloxane rings and coordinated to oxygen atoms from adjacent hydroxyl groups.[51] Thus, these findings suggest the predominance of grafted Ni^{2+} species on Ni–Li[Zn]Beta, consistent with CO IR spectra (Figure 1).

XANES spectra are shown in Figures S17 and S18 (Supporting Information) for Ni–H-[Al]Beta, Ni–Li-[Al]-Beta, and Ni–Li-[Zn]Beta under hydrated and dehydrated conditions and for Ni–Li-[Al]Beta during ethene dimerization (453 K, 0.07 kPa), with the results summarized in Table 2. Under both hydrated and dehydrated conditions, the pre-edge energy (Table 2) and pre-edge feature (Figure S18, Supporting Information) of Ni–H-[Al]Beta, Ni–Li-[Al]Beta, and Ni–Li-[Zn]Beta samples were the same as those of a NiO standard, indicating an oxidation state of +2, consistent with predominance of Ni^{2+} cations as indicated by the site balance (Table 1) and CO IR spectroscopy (Figure 1). Further, the XANES spectra collected for the dehydrated Ni–Li-[Al]Beta sample and the Ni–Li-[Al]Beta sample during reaction with ethene (453 K, 0.07 kPa) were identical (Figures S17 and S18), providing evidence for the prevalence of the +2 oxidation state for Ni during ethene dimerization catalysis, consistent with prior reports for propene oligomerization on Ni–X.[12]

The coordination geometry of Ni^{2+} cations was quantitatively assessed from the EXAFS region. Figures S19 and S20 (Supporting Information) show the EXAFS regions of the Ni–H-[Al]Beta and Ni–Li-[Al]Beta samples under hydrated and dehydrated conditions, and the results are summarized in Table 3. The fitted EXAFS model considered the first shell to represent Ni–O scatter and the second shell to represent either Ni–Si or Ni–Al scatter. The Ni–H-[Al]Beta and Ni–Li-[Al]Beta samples under hydrated and dehydrated conditions showed Ni–O coordination numbers of 6 and 4, respectively, indicating that Ni was present as octahedral $Ni^{2+}(H_2O)_6$ under hydrated conditions and as tetrahedral Ni^{2+} cations coordinated to framework oxygens after dehydration, consistent with DRUV spectra (Figure 2a,b). Further, Figure S21 (Supporting Information) shows the EXAFS region of the Ni–Li-[Zn]Beta sample under hydrated and dehydrated conditions, and the results are also summarized in Table 3.

Table 2. XANES Results for Ni–H-[Al]Beta, Ni–Li-[Al]Beta, and Ni–Li-[Zn]Beta Samples under Hydrated and Dehydrated Conditions and for Ni–Li-[Al]Beta during Ethene Dimerization (453 K, 0.07 kPa)

sample, condition	pre-edge energy (keV)	edge energy (keV)	oxidation state
Ni–H-[Al]Beta, hydrated	8.3333	8.3429	+2
Ni–H-[Al]Beta, dehydrated	8.3331	8.3406	+2
Ni–Li-[Al]Beta, hydrated	8.3333	8.3429	+2
Ni–Li-[Al]Beta, dehydrated	8.3331	8.3406	+2
Ni–Li-[Al]Beta, dimerization (453 K, 0.07 kPa ethene)	8.3331	8.3406	+2
Ni–Li-[Zn]Beta, hydrated	8.3332	8.3423	+2
Ni–Li-[Zn]Beta, dehydrated	8.3332	8.3423	+2
NiO, dehydrated	8.3332	8.3410	+2

Table 3. EXAFS Fitting Results for Ni–Li-[Al]Beta and Ni–Li-[Zn]Beta Samples under Hydrated and Dehydrated Conditions

sample, condition	scattering pair	coordination number	distance (Å)
Ni–H-[Al]Beta, hydrated	Ni–O	6.1 ± 0.1	2.04 ± 0.01
	Ni–Si/Al	1.7 ± 0.6	3.21 ± 0.02
Ni–H-[Al]Beta, dehydrated	Ni–O	4.7 ± 0.8	2.00 ± 0.02
	Ni–Si/Al	2.1 ± 0.2	2.74 ± 0.01
Ni–Li-[Al]Beta, hydrated	Ni–O	6.2 ± 0.4	2.04 ± 0.01
	Ni–Si/Al	1.6 ± 0.7	3.23 ± 0.02
Ni–Li-[Al]Beta, dehydrated	Ni–O	4.3 ± 0.2	2.00 ± 0.01
	Ni–Si/Al	1.9 ± 0.2	2.75 ± 0.01
Ni–Li-[Al]Beta, dimerization (453 K, 0.07 kPa ethene)	Ni–O	4.1 ± 0.2	2.00 ± 0.01
	Ni–Si/Al	2.0 ± 0.2	2.74 ± 0.01
Ni–Li-[Zn]Beta, hydrated	Ni–O	6.6 ± 0.4	2.04 ± 0.01
Ni–Li-[Zn]Beta, dehydrated	Ni–O	6.6 ± 0.4	2.04 ± 0.01
NiO, dehydrated	Ni–O	6.0	2.07 ± 0.01

The fitted EXAFS model considered the first shell to represent Ni–O scatter; however, no appropriate model was found to describe the second shell scatter. The hydrated and dehydrated Ni–Li-[Zn]Beta samples both showed a Ni–O coordination number of 6, consistent with the predominance of grafted Ni^{2+} species in Ni–Li[Zn]Beta, as evident from its DRUV (Figure 2c) and CO IR (Figure 1) spectra.

In summary, CO IR, DRUV, and XAS spectroscopies indicate that Ni is predominantly present as exchanged Ni^{2+} cations on Ni–H-[Al]Beta and Ni–Li-[Al]Beta and as grafted

DOI: 10.1021/acscatal.8b03202
ACS Catal. 2018, 8, 11407−11422

Ni^{2+} cations on Ni−Li-[Zn]Beta. In the dehydrated state and during ethene dimerization, Ni^{2+} cations in Ni−Li-[Al]Beta are four-coordinate and predominantly in distorted tetrahedral geometry according to UV−vis, XANES, and EXAFS data, consistent with the distorted tetrahedral environment of Ni^{2+} sites observed within the Ni-MFU-*4l* MOF material[85] that catalyzes ethene dimerization by the coordination−insertion mechanism.[24] Although Ni^{+} cations were observed in minority amounts on the Ni−H-[Al]Beta sample after vacuum treatment, such species are not expected to persist after an oxidative treatment. In addition, residual Brønsted acid sites were detected on Ni−H-[Al]Beta but not on Ni−Li-[Al]Beta, while the residual Brønsted acid sites detected on Ni−Li-[Zn]Beta are of weaker acid strength than those in aluminosilicates, as evident by their inability to protonate pyridine under equivalent conditions. Next, we use these model samples to probe the reaction pathways of ethene on Ni^{2+} cations and H^{+} sites.

3.3. Ethene Reaction Pathways on Ni^{2+} Cations and Brønsted Acid Sites. Scheme 1 shows a simplified representation of the metallacycle mechanism for ethene dimerization catalyzed by Ni^{δ} centers, where δ is the initial formal oxidation state. The catalytic cycle involves successive coordination of two ethene molecules, followed by two-electron oxidation of a Ni^{δ} center to form a $Ni^{\delta+2}$ metallacyclopentane complex, which undergoes β-hydride elimination and subsequent reductive elimination to form the terminal alkene (1-butene) as the predominant product.[22,29,86]

Scheme 1. Metallacycle Mechanism for Ethene Dimerization at a Ni^{δ} Active Site

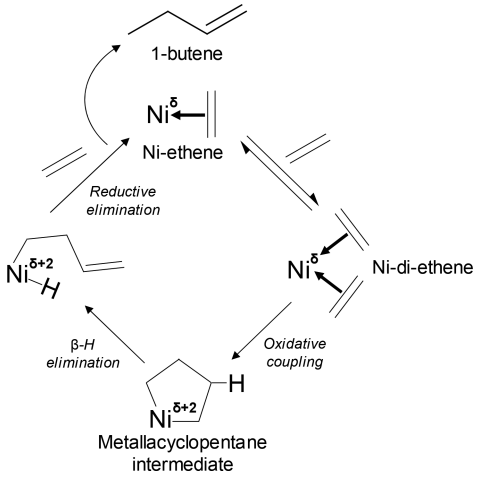

Scheme 2 shows a simplified representation of the coordination−insertion mechanism for ethene dimerization at [Ni(II)-H]$^{+}$ sites, first involving coordination and insertion of ethene into a Ni-hydride bond, and then into a Ni-alkyl bond, followed by β-hydride elimination to form 1-butene.[29] The formal Ni oxidation state is +2 for all reactive intermediates, and internal isomers (*cis*-2-butene, *trans*-2-butene) are also formed as primary reaction products by a parallel isomerization pathway.[28,30,31] In contrast to the metallacycle mechanism, the coordination−insertion mechanism is reported to be initiated by external activators for most homogeneous Ni systems,[87] except for methallyl[34] and SHOP-type[35] catalysts, it forms internal alkenes as primary products, and the Ni metal center

Scheme 2. Coordination−Insertion Mechanism for Ethene Dimerization at [Ni(II)-H]$^{+}$ Active Site[a]

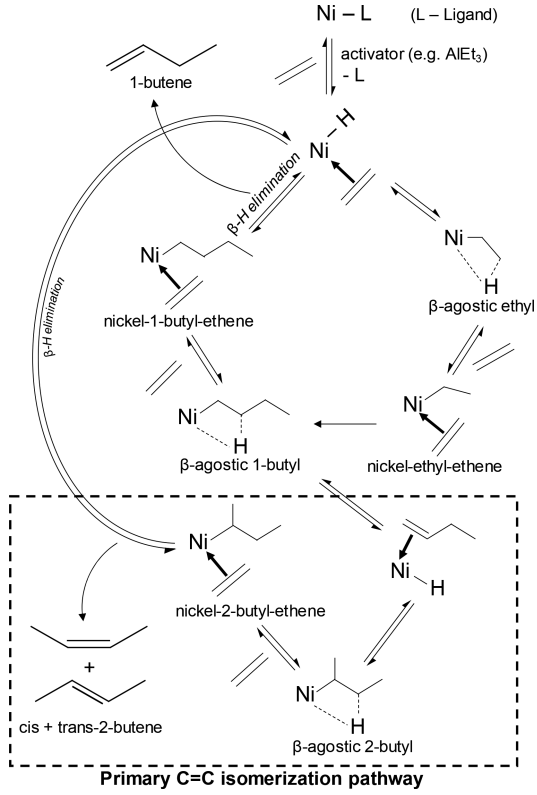

[a]The formal oxidation state of Ni is +2 for all Ni intermediates.

does not undergo a redox cycle. The key differences between the two mechanisms are summarized in Table 4.

Mechanistic studies for alkene dimerization catalysis using Ni^{2+} cations supported on aluminosilicates can be ambiguous when contributions from residual H^{+} sites convolute the analysis of alkene reaction pathways originating from Ni^{2+} sites. To discriminate the alkene reaction pathways originating from Ni^{2+} cations and H^{+} sites, 0.4 kPa of ethene was contacted at 453 K under differential conversion (<5%) with samples containing only H^{+} sites (H-[Al]Beta), both Ni^{2+} cations and H^{+} sites (Ni−H-[Al]Beta), both Ni^{2+} cations and trace amounts of residual H^{+} sites (Ni−Li-[Al]Beta) that have been further prepoisoned with NH_3 (Ni−Li-[Al]Beta-NH_3), and both Ni^{2+} cations and weaker residual H^{+} sites (Ni−Li-[Zn]Beta). Under these conditions (453 K, 0.4 kPa), ethene conversion increased during initial time for the Ni−Li-[Zn]Beta and Ni−Li-[Al]Beta-NH_3 samples (Figure S23, Supporting Information), while this activation behavior was not observed for the H-[Al]Beta, Ni−H-[Al]Beta, and Ni−Li-[Al]Beta samples (Figure S22, Supporting Information). On all

Table 4. Comparison between Coordination−Insertion and Metallacycle Mechanisms for Homogeneous Ni Complexes for Ethene Dimerization

	coordination−insertion	metallacycle
active site	[Ni(II)− H]$^{+}$	Ni^{δ}
activator requirement	needed in most cases	not needed
Ni oxidation state	+2	δ, δ+2
product selectivity	1-butene, *cis*-2-butene, *trans*-2-butene	1-butene

DOI: 10.1021/acscatal.8b03202
ACS Catal. 2018, 8, 11407−11422

samples, ethene conversion decreased with further time on stream (Figures S22 and S23, Supporting Information) indicating deactivation at long times.

Figure 3 shows product molar selectivities for H-[Al]Beta, Ni−H-[Al]Beta, Ni−Li-[Al]Beta, Ni−Li-[Al]Beta-NH_3, and

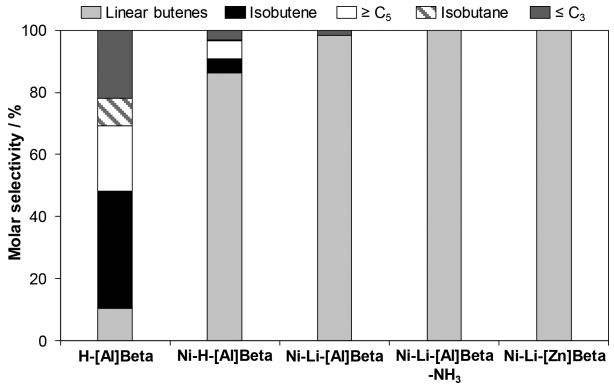

Figure 3. Product molar selectivities at 453 K, 0.4 kPa ethene for H-[Al]Beta (1.4% conv), Ni−H-[Al]Beta (1.4% conv), Ni−Li-[Al]Beta (1.4% conv), Ni−Li-[Zn]Beta (1.3% conv), and Ni−Li-[Al]Beta-NH_3 (without pretreatment) (1.6% conv). Flame ionization detection limit ≈ 0.02 ppm.

Ni−Li-[Zn]Beta at 453 K and 0.4 kPa ethene pressure. The product molar selectivities for Ni−Li-[Al]Beta-NH_3 and Ni−Li-[Zn]Beta were invariant with ethene conversion within differential ranges (<2%) (Figures S24 and S25, Supporting Information) while those for H-[Al]Beta, Ni−H-[Al]Beta, and Ni−Li-[Al]Beta changed with conversion (Figures S26−S28, Supporting Information) and thus are compared at iso-conversion values (1.4%) in Figure 3. All samples formed 1-butene, *cis*-2-butene, and *trans*-2-butene isomers (linear butenes). The H-[Al]Beta sample showed only 10% selectivity toward linear butenes, and formed significant amounts of isobutene, C_3 and smaller hydrocarbons, C_5 and larger hydrocarbons, and isobutane. The Ni−H-[Al]Beta sample predominantly formed linear butenes and smaller amounts of other products. The Ni−Li-[Al]Beta sample formed trace amounts of cracking products and isobutene, while the Ni−Li-[Al]Beta-NH_3 sample and the Ni−Li-[Zn]Beta sample selectively (>99%) formed linear butenes without any other detectable side products. These findings indicate that ethene dimerization to form linear butenes occurs on Ni^{2+} cations, while the H^+ sites present on [Al]Beta samples also catalyze the expected skeletal isomerization of dimer products to isobutene, along with cracking, oligomerization, and hydride transfer reactions.[88−93]

The linear butenes formed at Ni^{2+}-derived sites and H^+ sites consisted of 1-butene, *cis*-2-butene, and *trans*-2-butene isomers, suggesting that alkene double bond isomerization may be catalyzed by both types of sites. The two competing mechanisms (metallacycle and coordination−insertion) proposed for alkene dimerization on Ni cations differ in their selectivity toward the isomers of dimer products. In the case of dimerization of terminal alkenes (α-olefins), the metallacycle mechanism only forms terminal alkene dimers,[86] whereas the coordination−insertion mechanism forms both terminal and internal alkene dimers.[29] Moreover, the coordination−insertion mechanism involves a primary reaction route for forming internal alkene dimers, which does not require desorption and readsorption of terminal alkene dimers (Scheme 2). Therefore, to investigate the contributions of butene isomer formation, the ratios of 2-butenes/1-butene and isobutene/total butenes were measured (453 K, 0.2 kPa C_2H_4) as a function of reaction time on H-[Al]Beta, Ni−Li-[Al]Beta, and Ni−Li-[Zn]Beta. All samples deactivated under these conditions, as the ethene conversion decreased with reaction time (Figure S29, Supporting Information).

Figure 4a shows the 2-butenes/1-butene and isobutene/total butene ratios measured with reaction time on H-[Al]Beta (453 K, 0.2 kPa, 250 s (mol ethene)$^{-1}$ mol H^+), with a horizontal dashed line denoting the 2-butenes/1-butene ratio expected from thermodynamic equilibrium at 453 K (Section S.10, Supporting Information). Linear butenes were formed in equilibrated amounts at initial reaction times, but the 2-butenes/1-butene ratio decreased with time on stream, eventually reaching zero as the ethene conversion decreased to zero upon complete deactivation of H^+ sites (Figure S29a, Supporting Information). This decrease in 2-butenes/1-butene ratio was also concurrent with the decrease in the isobutene/total butenes ratio, consistent with the deactivation of H^+ sites that catalyze skeletal isomerization (Figure S29a, Supporting Information).

Figure 4b shows the 2-butenes/1-butene ratio and the isobutene/total butenes ratio, measured with reaction time on Ni−Li-[Al]Beta (453 K, 0.2 kPa, 2.4 s (mol ethene)$^{-1}$ mol Ni). In contrast to H-[Al]Beta, the initial 2-butenes/1-butene ratio measured at this site-time was lower than that expected from thermodynamic equilibrium, indicating that linear butenes were not quasi-equilibrated. Also, during initial reaction times,

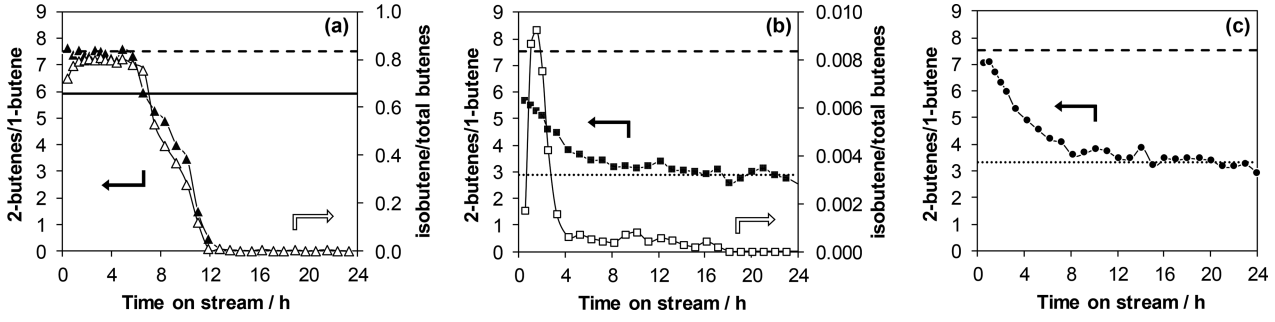

Figure 4. Variation of 2-butenes/1-butene ratio (filled symbols) and isobutene/total butenes ratio (unfilled symbols) for (a) H-[Al]Beta (▲) at 453 K, 0.2 kPa, 250 s (mol ethene)$^{-1}$ mol H^+, (b) Ni−Li-[Al]Beta (■) (453 K, 0.4 kPa, 2.4 s (mol ethene)$^{-1}$ mol Ni), and (c) Ni−Li-[Zn]Beta (●) (453 K, 0.7 kPa, 10.6 s (mol ethene)$^{-1}$ mol Ni). Lines are included to guide the eye: equilibrated 2-butenes/1-butene ratio at 453 K (– – – –), equilibrated isobutene/total butenes ratio at 453 K (—), and asymptotic steady-state 2-butenes/1-butene ratio (···).

DOI: 10.1021/acscatal.8b03202
ACS Catal. 2018, 8, 11407−11422

a small fraction of isobutene was detected (Figure 4b), attributed to skeletal isomerization on trace H^+ sites present below the detection limits of the characterization techniques used here (CO IR, AAS) or on H^+ sites generated in situ during Ni^{2+} activation to form $[Ni(II)\text{-}H]^+$ intermediates and proximal H^+ sites.[94] The 2-butenes/1-butene ratio for Ni−Li-[Al]Beta (Figure 4b) decreased with further time on stream, concurrent with a decrease in the isobutene/total butenes ratio, as expected from the deactivation of trace amounts of H^+ sites. Isobutene was no longer detectable after 12 h of reaction time, after which the 2-butenes/1-butene ratio reached a steady state but nonequilibrated value despite continued deactivation (Figure S29b, Supporting Information), indicating that butene double bond isomerization as solely catalyzed by the remaining Ni^{2+}-derived active sites as they continued to deactivate.

To confirm that butene double bond isomerization was catalyzed by Ni^{2+}-derived active sites, the 2-butenes/1-butene ratio was measured with reaction time on the Ni−Li-[Zn]Beta sample (453 K, 0.7 kPa, 10.6 s (mol ethene)$^{-1}$ mol Ni), as shown in Figure 4c. The 2-butenes/1-butene ratio decreased with reaction time to eventually reach a steady state but nonequilibrated value despite continued deactivation (Figure S29c, Supporting Information), similar to the observation on Ni−Li-[Al]Beta. No skeletal isomer products of butene were detected for Ni−Li-[Zn]Beta, although residual H^+ sites on [Zn]Beta formed double bond isomerization products, as also reported previously for propene oligomerization (453 K).[95] Therefore, the decrease in 2-butenes/1-butene ratio with time on stream for Ni−Li-[Zn]Beta may be attributed to the deactivation of residual H^+ sites, which mediate alkene double bond isomerization but not alkene skeletal isomerization under the conditions studied. The steady-state but nonequilibrium distribution of linear butenes on Ni−Li-[Al]Beta and Ni−Li-[Zn]Beta samples, after residual H^+ sites had deactivated, reflects butene double bond isomerization events that occur at Ni^{2+}-derived active sites.

Butene double bond isomerization on Ni−Li-[Al]Beta and Ni−Li-[Zn]Beta occur at both Ni^{2+}-derived and H^+ sites during initial reaction times, but only at remaining Ni^{2+}-derived sites at long time on stream, as denoted by the dotted lines in Figure 4 for the asymptotic limit for 2-butenes/1-butene ratio. To probe whether double bond isomerization pathways reflected primary or secondary reactions on Ni^{2+}-derived and H^+ sites, the reactant site-time was varied at fixed ethene pressure at 453 K. The effect of reactant site-time on the 2-butenes/1-butene ratio measured at initial reaction times, during which both Ni^{2+}-derived and H^+ sites are turning over, and on the 2-butenes/1-butene ratio measured in the asymptotic limit at long reaction times, during which only Ni^{2+}-derived sites are turning over, is shown in Figure 5a,b for Ni−Li-[Al]Beta and Ni−Li-[Zn]Beta, respectively. The asymptotic 2-butenes/1-butene ratio was invariant with site-time for Ni−Li-[Al]Beta and Ni−Li-[Zn]Beta, indicating that butene double bond isomerization on Ni^{2+}-derived sites occurs via primary pathways, consistent with the coordination−insertion mechanism. In contrast, the initial 2-butenes/1-butene ratio measured on Ni−Li-[Al]Beta increased with increasing site-time (Figure 5a), with a nonzero value upon extrapolation to zero site-time, consistent with a secondary reaction pathway for butene double bond isomerization on residual H^+ sites that occurs in parallel to a primary reaction pathway on Ni^{2+}-derived sites. The initial 2-butenes/1-butene ratio measured on Ni−Li-[Zn]Beta (Figure 5b) showed no discernible dependence on reactant site-time, because of the low conversion range studied here, precluding any conclusions about the nature of alkene double bond isomerization pathways at non-Ni^{2+}-derived sites on this sample.

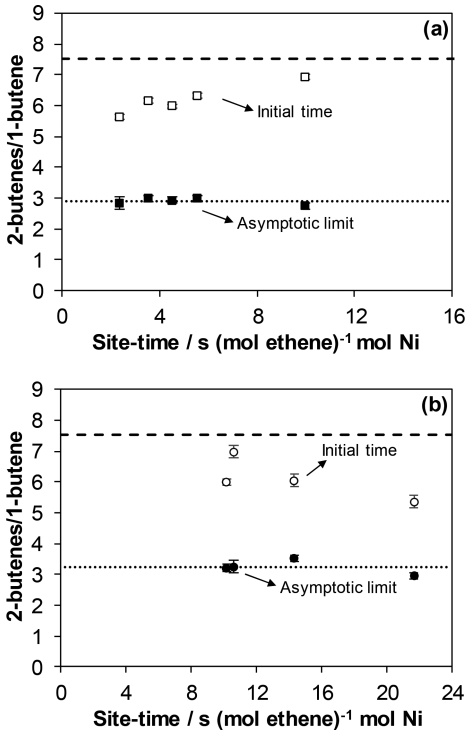

Figure 5. Effect of site-time on 2-butenes/1-butene ratio measured at 453 K during initial time on stream (hollow symbols) and after reaching asymptotic limit (filled symbols) for (a) Ni−Li-[Al]Beta (■) at 0.2 kPa and (b) Ni−Li-[Zn]Beta (●) at 0.7 kPa. Lines are included as guides: equilibrated 2-butenes/1-butene ratio at 453 K (– – –) and asymptotic steady-state 2-butenes/1-butene ratio (···).

Prior reports have proposed that Ni sites catalyze butene double bond isomerization on Ni−H-[Al]Y,[96] based on 1-butene selectivities among the C_4 products measured during pseudo steady state at long times on stream, after residual H^+ sites had presumably deactivated, which were similar to those measured on Ni−H-[Al]Y samples, whose H^+ sites were poisoned with NH_3 or pyridine. Yet, other reports (ethene oligomerization at 323−423 K on Ni−H-[Al]MCM-41,[15] Ni−H-[Al]MCM-22,[9] Ni−H-[Al]MCM-36,[9] Ni−H-[Al]USY,[45] and Ni−H-[Al]SBA-15[21]) propose 1-butene formation at Ni sites and secondary double-bond isomerization at H^+ sites, based on 1-butene selectivities that decrease with increasing H^+ site density and reactant site-time (ethene conversion). Although previously reported decreases in 1-butene selectivity with increasing site-time[21] are consistent with the observations in Figure 5a, the data and analysis presented here clarify that these observations reflect double bond isomerization via secondary reaction pathways at H^+ sites, which operate in parallel to a primary reaction pathway at Ni^{2+}-derived sites.

3.4. Active Site Structure and Formation in Absence of an Activator. Another distinction between the coordination−insertion and metallacycle mechanisms is the difference between their purported active site structures. Active sites for the coordination−insertion mechanism are proposed to be Ni(II)-hydride or Ni(II)-alkyl species, often generated from Ni^{2+} cations using external activators or initiators, while those

DOI: 10.1021/acscatal.8b03202
ACS Catal. 2018, 8, 11407−11422

for the metallacycle mechanism are also proposed to include reduced Ni states, whose formation does not require external activators. Both Ni−Li-[Al]Beta and Ni−Li-[Zn]Beta samples show evidence for coordination−insertion mechanism, even though external activators were absent, although Ni−Li-[Zn]Beta (but not Ni−Li-[Al]Beta) showed an activation transient at 453 K and 0.4 kPa ethene during initial reaction times (Figures S21 and S22, Supporting Information). This activation transient, however, was also observed for Ni−Li-[Al]Beta (Figure S30, Supporting Information) for ethene pressures below 0.4 kPa, while for Ni−Li-[Zn]Beta (Figure S31, Supporting Information) it was observed for all ethene pressures (0−1 kPa) studied.

The duration of the activation transient for Ni−Li-[Al]Beta at 453 K and fixed ethene pressure was invariant with ethene site-time at each pressure studied (Figure S32a, Supporting Information), while no discernible dependence on ethene site-time was observed for Ni−Li-[Zn]Beta (Figure S32b, Supporting Information). The activation period measured on Ni−Li-[Al]Beta decreased with increasing ethene pressure and was undetectable above 0.4 kPa, while that measured on Ni−Li-[Zn]Beta was invariant with ethene pressure, as shown in Figure 6. These findings are consistent with ethene-assisted

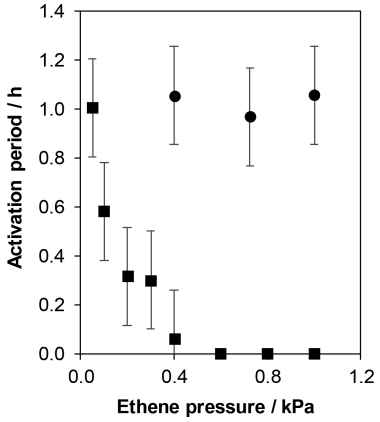

Figure 6. Effect of ethene pressure on activation period measured at 453 K for Ni−Li-[Al]Beta (■) and Ni−Li-[Zn]Beta (●).

formation of Ni-hydride intermediates in situ from exchanged Ni^{2+} cations on Ni−Li-[Al]Beta, as proposed by experiment to occur at Ni^{2+} cations in Ni−H-[Al]Beta via C−H bond activation of ethene to form Ni-ethenyl-hydride intermediates.[36] Density functional theory (DFT) (BEEF-vdW) studies[94] at Ni^{2+} cations in Ni-AFI have also proposed that the reaction of two ethene molecules followed by deprotonation leads to formation of a framework H^+ site and a [Ni(II)-butenyl]$^+$ complex, which then transforms into an agostic [Ni(II)-butadiene-H]$^+$ complex that undergoes β-hydride elimination (chain transfer) with ethene to form 1,3-butadiene and a [Ni(II)-hydride-ethene]$^+$ intermediate. In contrast to the behavior observed on Ni−Li-[Al]Beta, the weak effects of ethene pressure (in the range studied) on the duration of the activation period measured on Ni−Li-[Zn]Beta (Figure 6) likely reflects the presence of a minority amount of exchanged Ni^{2+} cations that form hydride intermediates.

To determine if the activation transient reflects the formation of [Ni(II)-H]$^+$ intermediates, butenes site-time yields were measured on Ni−Li-[Al]Beta and Ni−Li-[Zn]Beta in the presence of co-fed H_2 and were compared to those measured in the absence of co-fed H_2. Butenes site-time yields were taken as the sum of those for 1-butene, *cis*-2-butene, *trans*-2-butene, and isobutene (a secondary reaction product formed from linear butenes). Although the trace amounts of isobutene observed on Ni−Li-[Al]Beta suggest that minority H^+ sites are present that also catalyze ethene dimerization, their contributions to butenes site-time yields were assumed to be negligible, because initial site-time yields estimated (without co-fed H_2) at zero site-time on H-[Al]Beta (453 K, per H^+, Table S6) are 20× lower than those measured on Ni−Li-[Al]Beta (453 K, per Ni, Section S.13, Supporting Information). Also, the initial site-time yields measured on Ni−Li-[Zn]Beta (453 K, per Ni, Section S.13, Supporting Information) are 2 orders of magnitude lower than those on Ni−Li-[Al]Beta, indicating that the grafted octahedral Ni^{2+} cations predominantly present on Ni−Li-[Zn]Beta (2196 cm^{-1} CO IR, Figure 1c) are less reactive than the exchanged, tetrahedral Ni^{2+} cations present on Ni−Li-[Al]Beta. It is plausible that the minority charge-compensating Ni^{2+} cations present (2222 cm^{-1} CO IR, Figure 1c) are precursors to the dominant dimerization active sites on Ni−Li-[Zn]Beta.

Figure 7a,b shows the butenes site-time yield with time on stream for Ni−Li-[Al]Beta (0.05 kPa ethene, 453 K) and Ni−Li-[Zn]Beta (0.7 kPa ethene, 453 K), respectively, in the absence and presence of co-fed H_2 (5 kPa for Ni−Li-[Al]Beta and 7 kPa for Ni−Li-[Zn]Beta). In the absence of co-fed H_2,

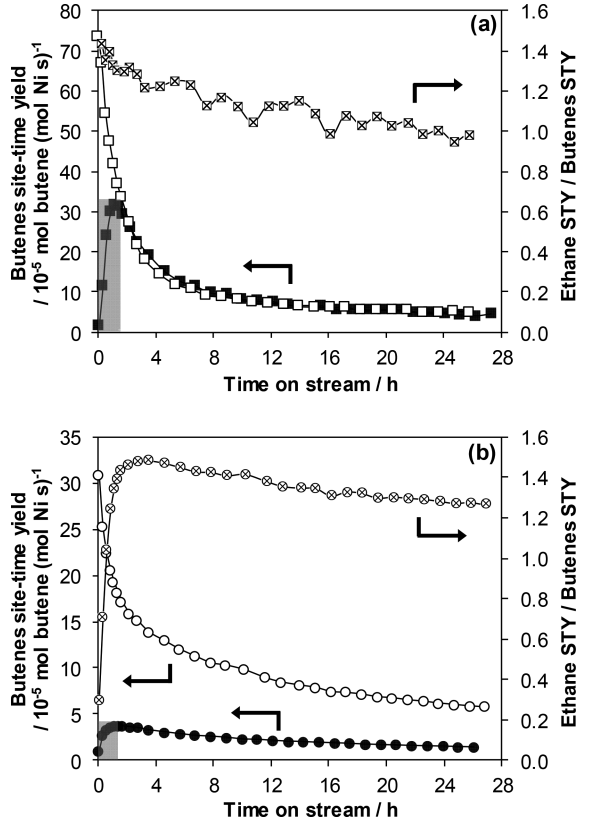

Figure 7. Butenes site-time yields at 453 K in the presence (hollow symbols) and absence (filled symbols) of H_2, and the ratio of site-time yields (STY) of ethane to butenes (symbols with cross), measured on (a) Ni−Li-[Al]Beta (■) at 0.05 kPa ethene, 11.1 s (mol ethene)$^{-1}$ mol Ni, 5 kPa H_2 and (b) Ni−Li-[Zn]Beta (●) at 0.7 kPa, 20 s (mol ethene)$^{-1}$ mol Ni, 7 kPa H_2. Lines are intended as guides, and the shaded region shows the activation period in absence of H_2.

DOI: 10.1021/acscatal.8b03202
ACS Catal. 2018, 8, 11407−11422

the butenes site-time yield on Ni−Li-[Al]Beta (Figure 7a) and Ni−Li-[Zn]Beta (Figure 7b) initially increased with time on stream during an activation period and then decreased during a deactivation period. A similar activation period was reported by Mlinar et. al[12] during initial reaction times for propene oligomerization on Ni−Na-[Al]X at 453 K, which was attributed to migration of Ni^{2+} cations from the hexagonal prisms of faujasite (FAU) to the sodalite cages and their coordination with propene to form a $[Ni(II)\text{-alkyl}]^+$ complex. Yet, this proposal seems unlikely for Ni^{2+} cations exchanged onto Beta frameworks that are located within 12-membered ring (12-MR) voids and accessible to alkene reactants. Further, in the presence of co-fed H_2, the activation transient was not observed for Ni−Li-[Al]Beta (Figure 7a) nor for Ni−Li-[Zn]Beta (Figure 7b), consistent with facilitated formation of $[Ni(II)\text{-H}]^+$ intermediates in the presence of H_2. Moreover, Ni−Li-[Al]Beta showed the same deactivation transient with and without co-fed H_2 after ∼5 h of time on stream (Figure 7a), indicating that a similar fraction of Ni^{2+} cations were transformed into active $[Ni(II)\text{-H}]^+$ intermediates in the presence and absence of H_2. In the case of Ni−Li-[Zn]Beta, butenes site-time yields were significantly higher in the presence of hydrogen (Figure 7b), which we surmise resulted in the formation of an increased number of active $[Ni(II)\text{-H}]^+$ intermediates from spectator Ni^{2+} cations that are predominantly grafted in the framework Beta, or in the formation of Zn-hydride intermediates that could also be active for ethene dimerization.

Co-fed H_2 also resulted in the formation of ethane as a side product via ethene hydrogenation. The ratio of ethane-to-butenes site-time yields is shown on the secondary axes of Figure 7a,b for Ni−Li-[Al]Beta (0.05 kPa C_2H_4, 5 kPa H_2, 453 K) and Ni−Li-[Zn]Beta (0.7 kPa C_2H_4, 7 kPa H_2, 453 K), respectively. This site-time yield ratio initially increased with time on stream for Ni−Li-[Zn]Beta but not for Ni−Li-[Al]Beta, and it decreased at longer times on stream to approach near unity values on both samples. This behavior is consistent with the presence of metal-hydride (Ni,[97] Zn,[98] Co[99]) intermediates, which have been reported to mediate alkene hydrogenation and alkane dehydrogenation cycles.

To further probe the formation of Ni-hydride intermediates in the presence of co-fed molecular hydrogen, H/D isotopic scrambling experiments were performed using different inlet H_2 and D_2 compositions at 453 K on Ni−Li-[Al]Beta and Ni−Li-[Zn]Beta, and on the Li-[Al]Beta, H-[Al]Beta, and Li-[Zn]Beta control samples. Ni−Li-[Al]Beta (Figure S37, Supporting Information) and Ni−Li-[Zn]Beta (Figure S38, Supporting Information) samples statistically scrambled the isotopic content of inlet H_2-D_2 mixtures in the effluent HD products, which was verified by comparisons to isotopic equilibration achieved in analogous H_2-D_2 scrambling experiments performed on a 1% Pt/Al_2O_3 sample (prereduced using H_2, 673 K, 1 h) (Figure S36, Supporting Information). Such isotopic scrambling was not observed on the control samples that did not contain Ni species (Li-[Al]Beta, H-[Al]Beta, Li-[Zn]Beta; Figures S37 and S38, Supporting Information).

The number of Ni^{2+} sites that reversibly form $[Ni(II)\text{-H}]^+$ or $[Ni(II)\text{-D}]^+$ intermediates (at 453 K) was estimated from sequential H_2-D_2 exchange experiments performed on Ni−Li-[Al]Beta and Ni−Li-[Zn]Beta (details in Section S.14.5, Supporting Information). Table 5 reports the amount of HD formed (per Ni site) on Ni−Li-[Al]Beta and Ni−Li-[Zn]Beta samples after each H_2/D_2 step change, after correcting for residual contributions from non-Ni sites measured on corresponding Li-exchanged control samples (details in Section S.14.6, Supporting Information). On average, the number of $[Ni(II)\text{-H}]^+$ intermediates was quantified to be 0.87 and 0.31 on Ni−Li-[Al]Beta and Ni−Li-[Zn]Beta, respectively (Table 5). The near unity value of 0.87 HD (per Ni) on Ni−Li-[Al]Beta reflects H−D exchange at nearly all Ni sites, which are predominantly present as exchanged Ni^{2+} cations (Sections 3.1 and 3.2). The subunity value of 0.30 HD (per Ni) on Ni−Li-[Zn]Beta reflects the presence of some grafted Ni^{2+} cations (Sections 3.1 and 3.2) that do not undergo H−D exchange under the conditions studied. Taken together, the H/D isotopic scrambling and H_2-D_2 exchange experiments provide quantitative evidence for the formation of $[Ni(II)\text{-H}]^+$ structures in the presence of H_2 at 453 K and provide justification for the elimination of activation transients on Ni−Li-[Al]Beta and Ni−Li-[Zn]Beta (Figure 7) in the presence of co-fed H_2.

Table 5. Quantification of Nickel Hydrides by Sequential H_2-D_2 Exchange Experiments at 453 K

	mol HD $(\text{mol Ni})^{-1}$		
catalyst	$H_2 \rightarrow D_2$	$D_2 \rightarrow H_2$	mol HD $(\text{mol Ni})^{-1}$ (average)
Ni−Li-[Al]Beta	0.92	0.85	0.87
	0.88	0.85	
	0.87	0.85	
Ni−Li-[Zn]Beta	0.32	0.32	0.31
	0.32	0.32	
	0.30	0.31	

4. CONCLUSIONS

Efforts to distinguish between metallacycle and coordination−insertion mechanisms for alkene dimerization catalyzed by Ni-based aluminosilicates are complicated, in part because residual H^+ sites on these supports also catalyze alkene dimerization and isomerization reactions. Ethene reaction pathways on Ni^{2+} cations and residual H^+ sites on aluminosilicate compositions of zeolite Beta were distinguished here by studying model materials that were prepared by progressively poisoning or weakening the strength of residual H^+ sites to suppress their reactivity. Ni^{2+}-derived sites selectively catalyze ethene dimerization to form linear butenes, while the H^+ sites on aluminosilicate Beta also catalyze cracking, oligomerization, hydride transfer, and skeletal isomerization of alkenes. Isobutene skeletal isomers of linear butenes were taken as a kinetic marker for the presence of residual H^+ sites, allowing discrimination of butene double bond isomerization pathways originating from H^+- and Ni^{2+}-derived sites. Double bond isomerization of 1-butene to 2-butene isomers occurred by secondary pathways on H^+ sites, but by primary reaction pathways on Ni^{2+}-derived sites, consistent with Ni-catalyzed coordination−insertion dimerization of ethene. Further, in situ X-ray absorption spectroscopy showed that Ni cations retained their +2 oxidation state during ethene dimerization, also consistent with coordination−insertion mechanism.

Ni^{2+} cations in Beta molecular sieves operate characteristically by the coordination−insertion mechanism of alkene dimerization in the absence of externally supplied activators or cocatalysts, although these are required to initiate coordination−insertion catalytic cycles in the case of α-diimine Ni complexes and Ni^{2+} cations supported on metal−organic frameworks. In the absence of external activators, an activation

DOI: 10.1021/acscatal.8b03202
ACS Catal. 2018, 8, 11407−11422

transient observed under dilute ethene conditions (<0.4 kPa) was eliminated by co-feeding H_2 to facilitate the in situ formation of $[Ni(II)\text{-}H]^+$ species, which are the proposed active sites in the coordination−insertion mechanism. The H_2-assisted formation of $[Ni(II)\text{-}H]^+$ species was verified by H/D isotopic scrambling, and H_2−D_2 isotopic exchange experiments quantified the number of $[Ni(II)\text{-}H]^+$ intermediates formed. In the absence of H_2 and external activators, the duration of the activation transient decreased with increasing ethene pressures, indicating that active Ni^{2+}-derived intermediates in the coordination−insertion mechanism are likely formed in situ upon reaction with ethene.

Taken together, alkene double bond isomerization at Ni^{2+} cations by a primary reaction pathway, the +2 oxidation state of Ni cations during dimerization catalysis, and the formation of $[Ni(II)\text{-}H]^+$ active intermediates, provide incontrovertible evidence for the dominance of coordination−insertion mechanism, and not the metallacycle mechanism, as the origin of alkene dimerization on Ni-exchanged zeolites. This implies that kinetic, and not thermodynamic, factors influence isomer distributions within alkene dimer products, providing an opportunity to influence the selectivity toward α-olefin isomers that are the desired comonomers in industrially practiced polymerization of ethene and propene.[100] Knowledge of the dominant reaction mechanism also provides a framework to interpret the kinetic effects of varying other catalyst structural features, such as the confining void environments around Ni^{2+} cations.

■ ASSOCIATED CONTENT

Supporting Information

The Supporting Information is available free of charge on the ACS Publications website at DOI: 10.1021/acscatal.8b03202.

Micropore volumes, ^{27}Al MAS NMR, SEM images, CO and pyridine infrared spectra, thermogravimetric analysis, XANES spectra, EXAFS fitted regions, nickel and cobalt ion-exchange isotherms, conversion versus reaction time, product selectivities versus conversion, activation period versus site-time, initial butenes site-time yields, H/D isotopic scrambling, H_2−D_2 exchange reactions, calculations for thermodynamic equilibrium of butene isomers and for statistical H/D distribution (PDF)

■ AUTHOR INFORMATION

Corresponding Author

*E-mail: rgounder@purdue.edu.

ORCID

Guanghui Zhang: 0000-0002-5854-6909
Jeffrey T. Miller: 0000-0002-6269-0620
Rajamani Gounder: 0000-0003-1347-534X

Notes

The authors declare no competing financial interest.

■ ACKNOWLEDGMENTS

Acknowledgment is made to the donors of the American Chemical Society Petroleum Research Fund for partial support of this research, under Grant No. 54216-DNI5. This work was also supported in part by the National Science Foundation under Cooperative Agreement No. EEC-1647722, an Engineering Research Center for the Innovative and Strategic Transformation of Alkane Resources. The use of Advanced Photon Source to obtain the XAS results is supported by the U.S. Department of Energy (DOE), Office of Science, and Office of Basic Energy Sciences, under Contract No. DE-AC02-06CH11357. MRCAT operations are supported by the DOE and the MRCAT member institutions. We also thank Prof. P. Stair (Northwestern) for helpful technical discussions.

■ REFERENCES

(1) Finiels, A.; Fajula, F.; Hulea, V. Nickel-Based Solid Catalysts for Ethylene Oligomerization - a Review. *Catal. Sci. Technol.* **2014**, *4*, 2412−2426.

(2) Nicholas, C. P. Applications of Light Olefin Oligomerization to the Production of Fuels and Chemicals. *Appl. Catal., A* **2017**, *543*, 82−97.

(3) Stangland, E. E. Shale Gas Implications for C_2-C_3 Olefin Production: Incumbent and Future Technology. *Annu. Rev. Chem. Biomol. Eng.* **2018**, *9*, 341−364.

(4) Bruijnincx, P. C. A.; Weckhuysen, B. M. Shale Gas Revolution: An Opportunity for the Production of Biobased Chemicals? *Angew. Chem., Int. Ed.* **2013**, *52*, 11980−11987.

(5) Bonneviot, L.; Olivier, D.; Che, M. Dimerization of Olefins with Nickel-Surface Complexes in X-Type Zeolite or on Silica. *J. Mol. Catal.* **1983**, *21*, 415−430.

(6) Cai, F. X.; Lepetit, C.; Kermarec, M.; Olivier, D. Dimerization of Ethylene into 1-Butene over Supported Tailor-made Nickel Catalysts. *J. Mol. Catal.* **1987**, *43*, 93−116.

(7) Heveling, J.; Nicolaides, C. P.; Scurrell, M. S. Catalysts and Conditions for the Highly Efficient, Selective and Stable Heterogeneous Oligomerisation of Ethylene. *Appl. Catal., A* **1998**, *173*, 1−9.

(8) Espinoza, R. L.; Nicolaides, C. P.; Korf, C. J.; Snel, R. Catalytic Oligomerization of Ethene over Nickel-Exchanged Amorphous Silica-Alumina; Effect of the Nickel Concentration. *Appl. Catal.* **1987**, *31*, 259−266.

(9) Lallemand, M.; Rusu, O. A.; Dumitriu, E.; Finiels, A.; Fajula, F.; Hulea, V. NiMCM-36 and NiMCM-22 Catalysts for the Ethylene Oligomerization: Effect of Zeolite Texture and Nickel Cations/Acid Sites Ratio. *Appl. Catal., A* **2008**, *338*, 37−43.

(10) Elev, I. V. The Role of Ni^+ Ions in the Activity of NiCaY Zeolite Catalysts for Ethylene Dimerization. *J. Catal.* **1984**, *89*, 470−477.

(11) Martínez, A.; Arribas, M. A.; Concepción, P.; Moussa, S. New Bifunctional Ni−H-Beta Catalysts for the Heterogeneous Oligomerization of Ethylene. *Appl. Catal., A* **2013**, *467*, 509−518.

(12) Mlinar, A. N.; Baur, G. B.; Bong, G. G.; Getsoian, A. B.; Bell, A. T. Propene Oligomerization over Ni-Exchanged Na-X Zeolites. *J. Catal.* **2012**, *296*, 156−164.

(13) Henry, R.; Komurcu, M.; Ganjkhanlou, Y.; Brogaard, R. Y.; Lu, L.; Jens, K. J.; Berlier, G.; Olsbye, U. Ethene Oligomerization on Nickel Microporous and Mesoporous-Supported Catalysts: Investigation of the Active Sites. *Catal. Today* **2018**, *299*, 154−163.

(14) Hartmann, M.; Pöppl, A.; Kevan, L. Ethylene Dimerization and Butene Isomerization in Nickel-Containing MCM-41 and AlMCM-41 Mesoporous Molecular Sieves: An Electron Spin Resonance and Gas Chromatography Study. *J. Phys. Chem.* **1996**, *100*, 9906−9910.

(15) Hulea, V.; Fajula, F. Ni-Exchanged AlMCM-41 - an Efficient Bifunctional Catalyst for Ethylene Oligomerization. *J. Catal.* **2004**, *225*, 213−222.

(16) Lallemand, M.; Finiels, A.; Fajula, F.; Hulea, V. Ethylene Oligomerization over Ni-Containing Mesostructured Catalysts with MCM-41, MCM-48 and SBA-15 Topologies. *Stud. Surf. Sci. Catal.* **2007**, *170*, 1863−1869.

(17) Mlinar, A. N.; Shylesh, S.; Ho, O. C.; Bell, A. T. Propene Oligomerization Using Alkali Metal- and Nickel-Exchanged Mesoporous Aluminosilicate Catalysts. *ACS Catal.* **2014**, *4*, 337−343.

(18) Zhang, Q.; Dalla Lana, I. G. An Analysis of Mass Transfer and Kinetics During Ethylene Oligomerization over Nickel/Sulfated Alumina Catalyst in a Slurry Reactor. *Chem. Eng. Sci.* **1997**, *52*, 4187−4195.

DOI: 10.1021/acscatal.8b03202
ACS Catal. 2018, 8, 11407−11422

(19) Zhang, Q.; Kantcheva, M.; Dalla Lana, I. G. Oligomerization of Ethylene in a Slurry Reactor Using a Nickel/Sulfated Alumina Catalyst. *Ind. Eng. Chem. Res.* **1997**, *36*, 3433−3438.
(20) Davydov, A. A.; Kantcheva, M.; Chepotko, M. L. FTIR Spectroscopic Study on Nickel(II)-Exchanged Sulfated Alumina: Nature of the Active Sites in the Catalytic Oligomerization of Ethene. *Catal. Lett.* **2002**, *83*, 97−108.
(21) Andrei, R. D.; Popa, M. I.; Fajula, F.; Hulea, V. Heterogeneous Oligomerization of Ethylene over Highly Active and Stable Ni-AlSBA-15 Mesoporous Catalysts. *J. Catal.* **2015**, *323*, 76−84.
(22) Grubbs, R. H.; Miyashita, A. Metallacyclopentanes as Catalysts for the Linear and Cyclodimerization of Olefins. *J. Am. Chem. Soc.* **1978**, *100*, 7416−7418.
(23) Grubbs, R. H.; Miyashita, A. The Metallacyclopentane−Olefin Interchange Reaction. *J. Chem. Soc., Chem. Commun.* **1977**, 864−865.
(24) Metzger, E. D.; Comito, R. J.; Hendon, C. H.; Dincă, M. Mechanism of Single-Site Molecule-Like Catalytic Ethylene Dimerization in Ni-MFU-4l. *J. Am. Chem. Soc.* **2017**, *139*, 757−762.
(25) Cossee, P. On the Reaction Mechanism of the Ethylene Polymerization with Heterogeneous Ziegler-Natta Catalysts. *Tetrahedron Lett.* **1960**, *1*, 12−16.
(26) Cossee, P. Ziegler-Natta Catalysis I. Mechanism of Polymerization of α-Olefins with Ziegler-Natta Catalysts. *J. Catal.* **1964**, *3*, 80−88.
(27) Arlman, E. J.; Cossee, P. Ziegler-Natta Catalysis III. Stereospecific Polymerization of Propene with the Catalyst System $TiCl_3$-$AlEt_3$. *J. Catal.* **1964**, *3*, 99−104.
(28) Svejda, S. A.; Brookhart, M. Ethylene Oligomerization and Propylene Dimerization Using Cationic (α-Diimine)Nickel(II) Catalysts. *Organometallics* **1999**, *18*, 65−74.
(29) Speiser, F.; Braunstein, P.; Saussine, L. Catalytic Ethylene Dimerization and Oligomerization: Recent Developments with Nickel Complexes Containing P,N-Chelating Ligands. *Acc. Chem. Res.* **2005**, *38*, 784−93.
(30) Skupinska, J. Oligomerization of α-Olefins to Higher Oligomers. *Chem. Rev.* **1991**, *91*, 613−648.
(31) Ittel, S. D.; Johnson, L. K.; Brookhart, M. Late-Metal Catalysts for Ethylene Homo- and Copolymerization. *Chem. Rev.* **2000**, *100*, 1169−1204.
(32) Britovsek, G. J. P.; Gibson, V. C.; Wass, D. F. The Search for New-Generation Olefin Polymerization Catalysts: Life Beyond Metallocenes. *Angew. Chem., Int. Ed.* **1999**, *38*, 428−447.
(33) Svejda, S. A.; Johnson, L. K.; Brookhart, M. Low-Temperature Spectroscopic Observation of Chain Growth and Migratory Insertion Barriers in (α-Diimine)Ni(II) Olefin Polymerization Catalysts. *J. Am. Chem. Soc.* **1999**, *121*, 10634−10635.
(34) Escobar, M. A.; Trofymchuk, O. S.; Rodriguez, B. E.; Lopez-Lira, C.; Tapia, R.; Daniliuc, C.; Berke, H.; Nachtigall, F. M.; Santos, L. S.; Rojas, R. S. Lewis Acid Enhanced Ethene Dimerization and Alkene Isomerization—ESI-MS Identification of the Catalytically Active Pyridyldimethoxybenzimidazole Nickel(II) Hydride Species. *ACS Catal.* **2015**, *5*, 7338−7342.
(35) Kuhn, P.; Semeril, D.; Matt, D.; Chetcuti, M. J.; Lutz, P. Structure-Reactivity Relationships in SHOP-Type Complexes: Tunable Catalysts for the Oligomerisation and Polymerisation of Ethylene. *Dalton Transactions* **2007**, 515−528.
(36) Moussa, S.; Concepción, P.; Arribas, M. A.; Martínez, A. Nature of Active Nickel Sites and Initiation Mechanism for Ethylene Oligomerization on Heterogeneous Ni-Beta Catalysts. *ACS Catal.* **2018**, *8*, 3903−3912.
(37) Sarazen, M. L.; Doskocil, E.; Iglesia, E. Effects of Void Environment and Acid Strength on Alkene Oligomerization Selectivity. *ACS Catal.* **2016**, *6*, 7059−7070.
(38) Alvarado Perea, L.; Wolff, T.; Veit, P.; Hilfert, L.; Edelmann, F. T.; Hamel, C.; Seidel-Morgenstern, A. Alumino-Mesostructured Ni Catalysts for the Direct Conversion of Ethene to Propene. *J. Catal.* **2013**, *305*, 154−168.
(39) Shephard, F. E.; Rooney, J. J.; Kemball, C. The Polymerization of Propylene on Silica-Alumina. *J. Catal.* **1962**, *1*, 379−388.
(40) Pines, H. In *The Chemistry of Catalytic Hydrocarbon Conversions;* Academic Press: New York, 1981; p 6.
(41) Hartmann, M.; Pöppl, A.; Kevan, L. Ethylene Dimerization in Nickel Containing MCM-41 and AlMCM-41 Studied by Electron Spin Resonance and Gas Chromatography. *Stud. Surf. Sci. Catal.* **1996**, *101*, 801−809.
(42) Ghosh, A. K.; Kevan, L. Electron Spin Resonance Studies of Ethylene Dimerization Catalyzed by Nickel Species on Y Zeolites. *J. Phys. Chem.* **1990**, *94*, 3117−3121.
(43) Lallemand, M.; Finiels, A.; Fajula, F.; Hulea, V. Nature of the Active Sites in Ethylene Oligomerization Catalyzed by Ni-Containing Molecular Sieves: Chemical and IR Spectral Investigation. *J. Phys. Chem. C* **2009**, *113*, 20360−20364.
(44) Agirrezabal-Telleria, I.; Iglesia, E. Stabilization of Active, Selective, and Regenerable Ni-Based Dimerization Catalysts by Condensation of Ethene Withinordered Mesopores. *J. Catal.* **2017**, *352*, 505−514.
(45) Lallemand, M.; Finiels, A.; Fajula, F.; Hulea, V. Catalytic Oligomerization of Ethylene over Ni-Containing Dealuminated Y Zeolites. *Appl. Catal., A* **2006**, *301*, 196−201.
(46) Lallemand, M.; Finiels, A.; Fajula, F.; Hulea, V. Continuous Stirred Tank Reactor for Ethylene Oligomerization Catalyzed by NiMCM-41. *Chem. Eng. J.* **2011**, *172*, 1078−1082.
(47) Toch, K.; Thybaut, J. W.; Arribas, M. A.; Martínez, A.; Marin, G. B. Steering Linear 1-Alkene, Propene or Gasoline Yields in Ethene Oligomerization via the Interplay between Nickel and Acid Sites. *Chem. Eng. Sci.* **2017**, *173*, 49−59.
(48) Takewaki, T.; Beck, L. W.; Davis, M. E. Zincosilicate CIT-6: A Precursor to a Family of *BEA-Type Molecular Sieves. *J. Phys. Chem. B* **1999**, *103*, 2674−2679.
(49) Yonemitsu, M.; Tanaka, Y.; Iwamoto, M. Metal Ion-Planted MCM-41. 1. Planting of Manganese(II) Ion into MCM-41 by a Newly Developed Template-Ion Exchange Method. *Chem. Mater.* **1997**, *9*, 2679−2681.
(50) Ikeda, K.; Kawamura, Y.; Yamamoto, T.; Iwamoto, M. Effectiveness of the Template-Ion Exchange Method for Appearance of Catalytic Activity of Ni−MCM-41 for the Ethene to Propene Reaction. *Catal. Commun.* **2008**, *9*, 106−110.
(51) Tanaka, M.; Itadani, A.; Kuroda, Y.; Iwamoto, M. Effect of Pore Size and Nickel Content of Ni-MCM-41 on Catalytic Activity for Ethene Dimerization and Local Structures of Nickel Ions. *J. Phys. Chem. C* **2012**, *116*, 5664−5672.
(52) Cybulskis, V. J.; Harris, J. W.; Zvinevich, Y.; Ribeiro, F. H.; Gounder, R. A Transmission Infrared Cell Design for Temperature-Controlled Adsorption and Reactivity Studies on Heterogeneous Catalysts. *Rev. Sci. Instrum.* **2016**, *87*, 103−101.
(53) Harris, J. W.; Cordon, M. J.; Di Iorio, J. R.; Vega-Vila, J. C.; Ribeiro, F. H.; Gounder, R. Titration and Quantification of Open and Closed Lewis Acid Sites in Sn-Beta Zeolites that Catalyze Glucose Isomerization. *J. Catal.* **2016**, *335*, 141−154.
(54) Pazmiño, J. H.; Shekhar, M.; Damion Williams, W.; Cem Akatay, M.; Miller, J. T.; Nicholas Delgass, W.; Ribeiro, F. H. Metallic Pt as Active Sites for the Water−Gas Shift Reaction on Alkali-Promoted Supported Catalysts. *J. Catal.* **2012**, *286*, 279−286.
(55) Kuehl, G. H.; Timken, H. K. C. Acid Sites in Zeolite Beta: Effects of Ammonium Exchange and Steaming. *Microporous Mesoporous Mater.* **2000**, *35*, 521−532.
(56) Bourgeat-Lami, E.; Massiani, P.; Di Renzo, F.; Espiau, P.; Fajula, F.; Des Courières, T. Study of the State of Aluminium in Zeolite-β. *Appl. Catal.* **1991**, *72*, 139−152.
(57) Woolery, G. L.; Kuehl, G. H.; Timken, H. C.; Chester, A. W.; Vartuli, J. C. On the Nature of Framework Brønsted and Lewis Acid Sites in ZSM-5. *Zeolites* **1997**, *19*, 288−296.
(58) Dědeček, J.; Sobalík, Z.; Wichterlová, B. Siting and Distribution of Framework Aluminium Atoms in Silicon-Rich Zeolites and Impact on Catalysis. *Catal. Rev.: Sci. Eng.* **2012**, *54*, 135−223.
(59) Abraham, A.; Lee, S.-H.; Shin, C.-H.; Bong Hong, S.; Prins, R.; van Bokhoven, J. A. Influence of Framework Silicon to Aluminium Ratio on Aluminium Coordination and Distribution in Zeolite Beta

DOI: 10.1021/acscatal.8b03202
ACS Catal. 2018, 8, 11407−11422

Investigated by ^{27}Al MAS and ^{27}Al MQ MAS NMR. *Phys. Chem. Chem. Phys.* **2004**, *6*, 3031−3036.
(60) Orazov, M.; Davis, M. E. Catalysis by Framework Zinc in Silica-Based Molecular Sieves. *Chem. Sci.* **2016**, *7*, 2264−2274.
(61) Mintova, S.; Valtchev, V.; Onfroy, T.; Marichal, C.; Knözinger, H.; Bein, T. Variation of the Si/Al Ratio in Nanosized Zeolite Beta Crystals. *Microporous Mesoporous Mater.* **2006**, *90*, 237−245.
(62) Hadjiivanov, K.; Penkova, A.; Centeno, M. A. FTIR Indication of CO Interaction with O^{2-} Ions: A New Adsorption Form in the Gap between Chemi- and Physisorbed CO. *Catal. Commun.* **2007**, *8*, 1715−1718.
(63) Maache, M.; Janin, A.; Lavalley, J. C.; Joly, J. F.; Benazzi, E. Acidity of Zeolites Beta Dealuminated by Acid Leaching: An FTi.r. Study Using Different Probe Molecules (Pyridine, Carbon Monoxide). *Zeolites* **1993**, *13*, 419−426.
(64) Zecchina, A.; Scarano, D.; Bordiga, S.; Spoto, G.; Lamberti, C. Surface Structures of Oxides and Halides and Their Relationships to Catalytic Properties. In *Advances in Catalysis;* Academic Press: New York, 2001; Vol. *46*, p 265.
(65) Mihaylov, M.; Hadjiivanov, K.; Knözinger, H. Formation of $Ni(CO)_4$ During the Interaction between CO and Silica-Supported Nickel Catalyst: An FTIR Spectroscopic Study. *Catal. Lett.* **2001**, *76*, 59−63.
(66) Aleksandrov, H. A.; Zdravkova, V. R.; Mihaylov, M. Y.; Petkov, P. S.; Vayssilov, G. N.; Hadjiivanov, K. I. Precise Identification of the Infrared Bands of the Polycarbonyl Complexes on Ni−MOR Zeolite by $^{12}C^{16}O-^{13}C^{18}O$ Coadsorption and Computational Modeling. *J. Phys. Chem. C* **2012**, *116*, 22823−22831.
(67) Penkova, A.; Dzwigaj, S.; Kefirov, R.; Hadjiivanov, K.; Che, M. Effect of the Preparation Method on the State of Nickel Ions in BEA Zeolites. A Study by Fourier Transform Infrared Spectroscopy of Adsorbed CO and NO, Temperature-Programmed Reduction, and X-Ray Diffraction. *J. Phys. Chem. C* **2007**, *111*, 8623−8631.
(68) Mihaylov, M.; Hadjiivanov, K. FTIR Study of CO and NO Adsorption and Coadsorption on Ni-ZSM-5 and Ni/SiO_2. *Langmuir* **2002**, *18*, 4376−4383.
(69) Hadjiivanov, K.; Knözinger, H.; Mihaylov, M. FTIR Study of CO Adsorption on Ni-ZSM-5. *J. Phys. Chem. B* **2002**, *106*, 2618−2624.
(70) Ganjkhanlou, Y.; Groppo, E.; Bordiga, S.; Volkova, M. A.; Berlier, G. Incorporation of Ni into HZSM-5 Zeolites: Effects of Zeolite Morphology and Incorporation Procedure. *Microporous Mesoporous Mater.* **2016**, *229*, 76−82.
(71) Knozinger, H.; Huber, S. IR Spectroscopy of Small and Weakly Interacting Molecular Probes for Acidic and Basic Zeolites. *J. Chem. Soc., Faraday Trans.* **1998**, *94*, 2047−2059.
(72) Góra-Marek, K.; Glanowska, A.; Datka, J. Quantitative IR Studies of the Concentration of Different Nickel Sites in NiZSM-5 Zeolites. *Microporous Mesoporous Mater.* **2012**, *158*, 162−169.
(73) Stolper, E. Water in Silicate Glasses: An Infrared Spectroscopic Study. *Contrib. Mineral. Petrol.* **1982**, *81*, 1−17.
(74) Li, D.; Nishijima, A.; Morris, D. E. Zeolite-Supported Ni and Mo Catalysts for Hydrotreatments: I. Catalytic Activity and Spectroscopy. *J. Catal.* **1999**, *182*, 339−348.
(75) Ballhausen, C. J. In *Introduction to Ligand Field Theory;* McGraw-Hill: New York, 1962; p 261.
(76) Jørgensen, C. K.; et al. Comparative Crystal Field Studies. 2. Nickel (II) and Copper (II) Complexes with Poyldentate Ligands and the Behaviour of the Residual Places for Co-ordination. *Acta Chem. Scand.* **1956**, *10*, 887−910.
(77) Jørgensen, C. K.; Smith, L. H.; Hanshoff, G.; Prydz, H. Comparative Crystal Field Studies of Some Ligands and the Lowest Singlet State of Paramagnetic Nickel(II) Complexes. *Acta Chem. Scand.* **1955**, *9*, 1362−1377.
(78) Lever, A. B. P. In *Inorganic Electronic Spectroscopy,* 2nd ed.; Elsevier: Amsterdam, The Netherlands, 1984; Vol. 33, p 507.
(79) Baran, R.; Śrębowata, A.; Kamińska, I. I.; Łomot, D.; Dzwigaj, S. Catalytic Activity of HAlBEA and Ni_xHAlBEA Zeolites in Hydrogen-Assisted Dehydrochlorination of 1,2-Dichloroethane into Vinyl Chloride Monomer. *Microporous Mesoporous Mater.* **2013**, *180*, 209−218.
(80) Śrębowata, A.; Baran, R.; Łomot, D.; Lisovytskiy, D.; Onfroy, T.; Dzwigaj, S. Remarkable Effect of Postsynthesis Preparation Procedures on Catalytic Properties of Ni-Loaded BEA Zeolites in Hydrodechlorination of 1,2-Dichloroethane. *Appl. Catal., B* **2014**, *147*, 208−220.
(81) Zanjanchi, M. A.; Ebrahimian, A. A Complementary Spectroscopic Study on the Nickel-Containing Zeolite Y Modified by Solid-State Dealumination. *Mater. Chem. Phys.* **2008**, *110*, 228−233.
(82) Lepetit, C.; Che, M. Discussion on the Coordination of Ni^{2+} Ions to Lattice Oxygens in Calcined Faujasite-Type Zeolites Followed by Diffuse Reflectance Spectroscopy. *J. Phys. Chem.* **1996**, *100*, 3137−3143.
(83) Olivier, D.; Bonneviot, L.; Cai, F.; Che, M.; Gihr, P.; Kermarec, M.; Lepetitpourcelot, C.; Morin, B. Preparation, Characterization and Reactivity of Complex Ni(I) Ions Supported on Silica. *Bull. Soc. Chim. Fr.* **1985**, 370−380.
(84) Klier, K.; Rálek, M. Spectra of Zynthetic Zeolites Containing Transition Metal Ions—II. Ni^{2+} Ions in Type a Linde Molecular Sieves. *J. Phys. Chem. Solids* **1968**, *29*, 951−957.
(85) Comito, R. J.; Metzger, E. D.; Wu, Z.; Zhang, G.; Hendon, C. H.; Miller, J. T.; Dincă, M. Selective Dimerization of Propylene with Ni-MFU-4 L. *Organometallics* **2017**, *36*, 1681−1683.
(86) McGuinness, D. S. Olefin Oligomerization via Metallacycles: Dimerization, Trimerization, Tetramerization, and Beyond. *Chem. Rev.* **2011**, *111*, 2321−2341.
(87) Bryliakov, K. P.; Antonov, A. A. Recent Progress of Transition Metal Based Catalysts for the Selective Dimerization of Ethylene. *J. Organomet. Chem.* **2018**, *867*, 55−61.
(88) Sanati, M.; Hornell, C.; Jaras, S. G. The Oligomerization of Alkenes by Heterogeneous Catalysts. In *Catalysis;* The Royal Society of Chemistry: Cambridge, U.K., 1999; Vol. *14*, p 236.
(89) Datka, J. Transformations of Butenes on Dehydroxylated Y Zeolites Studied by Infrared Spectroscopy. *J. Chem. Soc., Faraday Trans. 1* **1981**, *77*, 2633−2643.
(90) Kustov, L. M.; Borovkov, V. Y.; Kazansky, V. B. Study of Ethylene Oligomerization on Bronsted and Lewis Acidic Sites of Zeolites Using Diffuse Reflectance IR Spectroscopy. *Stud. Surf. Sci. Catal.* **1984**, *18*, 241−247.
(91) Miller, S. J. Olefin Oligomerization over High Silica Zeolites. *Stud. Surf. Sci. Catal.* **1988**, *38*, 187−197.
(92) Quann, R. J.; Green, L. A.; Tabak, S. A.; Krambeck, F. J. Chemistry of Olefin Oligomerization over ZSM-5 Catalyst. *Ind. Eng. Chem. Res.* **1988**, *27*, 565−570.
(93) Feller, A.; Barth, J.-O.; Guzman, A.; Zuazo, I.; Lercher, J. A. Deactivation Pathways in Zeolite-Catalyzed Isobutane/Butene Alkylation. *J. Catal.* **2003**, *220*, 192−206.
(94) Brogaard, R. Y.; Olsbye, U. Ethene Oligomerization in Ni-Containing Zeolites: Theoretical Discrimination of Reaction Mechanisms. *ACS Catal.* **2016**, *6*, 1205−1214.
(95) Deimund, M. A.; Labinger, J.; Davis, M. E. Nickel-Exchanged Zincosilicate Catalysts for the Oligomerization of Propylene. *ACS Catal.* **2014**, *4*, 4189−4195.
(96) Ng, F. T. T.; Creaser, D. C. Ethylene Dimerization over Modified Nickel Exchanged Y-Zeolite. *Appl. Catal., A* **1994**, *119*, 327−339.
(97) Zhang, G.; Yang, C.; Miller, J. T. Tetrahedral Nickel(II) Phosphosilicate Single-Site Selective Propane Dehydrogenation Catalyst. *ChemCatChem* **2018**, *10*, 961−964.
(98) Schweitzer, N. M.; Hu, B.; Das, U.; Kim, H.; Greeley, J.; Curtiss, L. A.; Stair, P. C.; Miller, J. T.; Hock, A. S. Propylene Hydrogenation and Propane Dehydrogenation by a Single-Site Zn^{2+} on Silica Catalyst. *ACS Catal.* **2014**, *4*, 1091−1098.
(99) Estes, D. P.; Siddiqi, G.; Allouche, F.; Kovtunov, K. V.; Safonova, O. V.; Trigub, A. L.; Koptyug, I. V.; Copéret, C. C−H Activation on Co_3O Sites: Isolated Surface Sites Versus Molecular Analogs. *J. Am. Chem. Soc.* **2016**, *138*, 14987−14997.

DOI: 10.1021/acscatal.8b03202
ACS Catal. 2018, 8, 11407−11422

(100) Forestière, A.; Olivier-Bourbigou, H.; Saussine, L. Oligomerization of Monoolefins by Homogeneous Catalysts. *Oil Gas Sci. Technol.* **2009**, *64*, 649−667.

DOI: 10.1021/acscatal.8b03202
ACS Catal. 2018, 8, 11407−11422